iScience

CellPress
OPEN ACCESS

Article

Redox-dependent condensation and cytoplasmic granulation by human ssDNA-binding protein-1 delineate roles in oxidative stress response

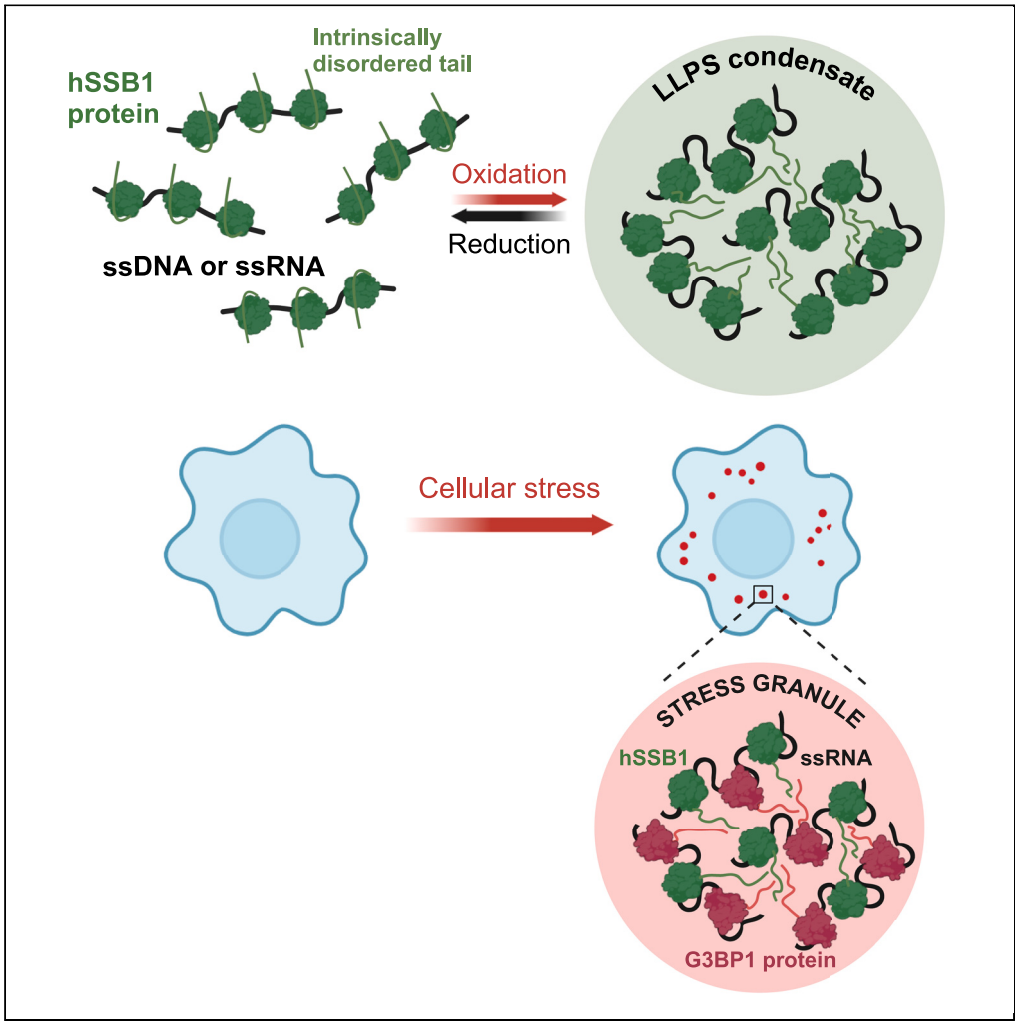

Gábor M. Harami, János Pálinkás, Zoltán J. Kovács, ..., Szilárd Tóth, Gergely Szakács, Mihály Kovács

mihaly.kovacs@ttk.elte.hu

Highlights

hSSB1 forms nucleoprotein coacervates via LLPS under oxidative conditions

All cysteines of hSSB1 are required for redox-dependent LLPS propensity

Interaction partners of hSSB1 are selectively enriched in hSSB1 droplets

Cytoplasmic hSSB1 condensates colocalize with stress granules upon cellular stress

Harami et al., iScience 27, 110788
September 20, 2024
https://doi.org/10.1016/j.isci.2024.110788

iScience

CellPress
OPEN ACCESS

Article

Redox-dependent condensation and cytoplasmic granulation by human ssDNA-binding protein-1 delineate roles in oxidative stress response

Gábor M. Harami,[1,6,7] János Pálinkás,[1,7] Zoltán J. Kovács,[1,2,7] Bálint Jezsó,[1,7] Krisztián Tárnok,[3] Hajnalka Harami-Papp,[1,6] József Hegedüs,[1] Lamiya Mahmudova,[1] Nóra Kucsma,[4] Szilárd Tóth,[4] Gergely Szakács,[4,5] and Mihály Kovács[1,2,8,*]

SUMMARY

Human single-stranded DNA binding protein 1 (hSSB1/NABP2/OBFC2B) plays central roles in DNA repair. Here, we show that purified hSSB1 undergoes redox-dependent liquid-liquid phase separation (LLPS) in the presence of single-stranded DNA or RNA, features that are distinct from those of LLPS by bacterial SSB. hSSB1 nucleoprotein droplets form under physiological ionic conditions in response to treatment modeling cellular oxidative stress. hSSB1's intrinsically disordered region is indispensable for LLPS, whereas all three cysteine residues of the oligonucleotide/oligosaccharide-binding fold are necessary to maintain redox-sensitive droplet formation. Proteins interacting with hSSB1 show selective enrichment inside hSSB1 droplets, suggesting tight content control and recruitment functions for the condensates. While these features appear instrumental for genome repair, we detected cytoplasmic hSSB1 condensates in various cell lines colocalizing with stress granules upon oxidative stress, implying extranuclear function in cellular stress response. Our results suggest condensation-linked roles for hSSB1, linking genome repair and cytoplasmic defense.

INTRODUCTION

Single-stranded (ss) DNA binding (SSB) proteins are found in all living organisms.[1] Their main function is the binding and stabilization of exposed ssDNA regions that form during DNA metabolic processes including replication, recombination, and repair.[2] Protection of ssDNA regions from nucleolytic cleavage, unproductive secondary structure formation and harmful chemical alterations is essential for genome integrity. Moreover, SSBs specifically interact with several other proteins participating in genome maintenance, conferring an organizing hub function for SSBs in DNA metabolism.[1,3] A 19-kDa subunit of the "prototypic" homotetrameric SSB of *Escherichia coli* (EcSSB) comprises an N-terminal oligonucleotide/oligosaccharide binding (OB) fold followed by an intrinsically disordered region (IDR)[4] (Figure 1A). Besides mitochondrial SSB, the heterotrimeric replication protein A (RPA) was considered as the only functional metazoan SSB until the discovery of SSB homologs SSB1 and SSB2 (termed hSSB1/NABP2/OBFC2B and hSSB2/NABP1/OBFC2A, respectively, in humans).[5] hSSB1 and hSSB2 share high structural similarity to EcSSB, having an N-terminal OB fold followed by C-terminal IDR (Figures 1A and 1B).[4,6] hSSB1 is expressed ubiquitously in human tissues, while hSSB2 expression is tissue specific, restricted mainly to immune cells and testes.[7] Growing evidence highlights central functions for hSSB1 in DNA repair,[8] telomere maintenance,[9] RNA transcription,[10] and embryonic development.[11] While hSSB1 appears to perform wide-ranging cellular functions, most of our knowledge comes from studies focusing on its DNA repair function. hSSB1 was shown to be an early sensor of DNA damage upon ionizing radiation (IR), whereby it localizes to DNA double-strand break (DSB) repair foci and organizes subsequent homologous recombination (HR) mediated DNA repair.[5,12] hSSB1 facilitates DNA end resection, an early step in HR, by recruiting the MRN complex[13] and stimulating Exo1 activity.[14] D-loop formation by RAD51 recombinase, a key step in early HR, is also facilitated by hSSB1.[5] hSSB1 colocalizes with Bloom's syndrome helicase (BLM) on IR-induced DSBs.[15] While hSSB1 is dispensable for normal S-phase DNA replication, it is required for stabilization and restart of replication forks that collapse upon hydroxyurea treatment.[16] Another major role of hSSB1 is exerted during the repair of oxidative DNA damage (such as formation of 8-oxoguanine) via the

[1]ELTE-MTA "Momentum" Motor Enzymology Research Group, Department of Biochemistry, Eötvös Loránd University, Pázmány P. s. 1/c, 1117 Budapest, Hungary
[2]HUN-REN-ELTE Motor Pharmacology Research Group, Department of Biochemistry, Eötvös Loránd University, Pázmány P. s. 1/c, 1117 Budapest, Hungary
[3]Department of Physiology and Neurobiology, Eötvös Loránd University, Pázmány P. s. 1/c, 1117 Budapest, Hungary
[4]HUN-REN Institute of Molecular Life Sciences, Research Centre for Natural Sciences, Magyar Tudósok körútja 2, 1117 Budapest, Hungary
[5]Center for Cancer Research, Medical University of Vienna, Borschkegasse 8a, 1090 Wien, Austria
[6]Present address: Laboratory of Single Molecule Biophysics, National Heart, Lung and Blood Institute, National Institutes of Health, Bethesda, Maryland 20892, USA
[7]These authors contributed equally
[8]Lead contact
*Correspondence: mihaly.kovacs@ttk.elte.hu
https://doi.org/10.1016/j.isci.2024.110788

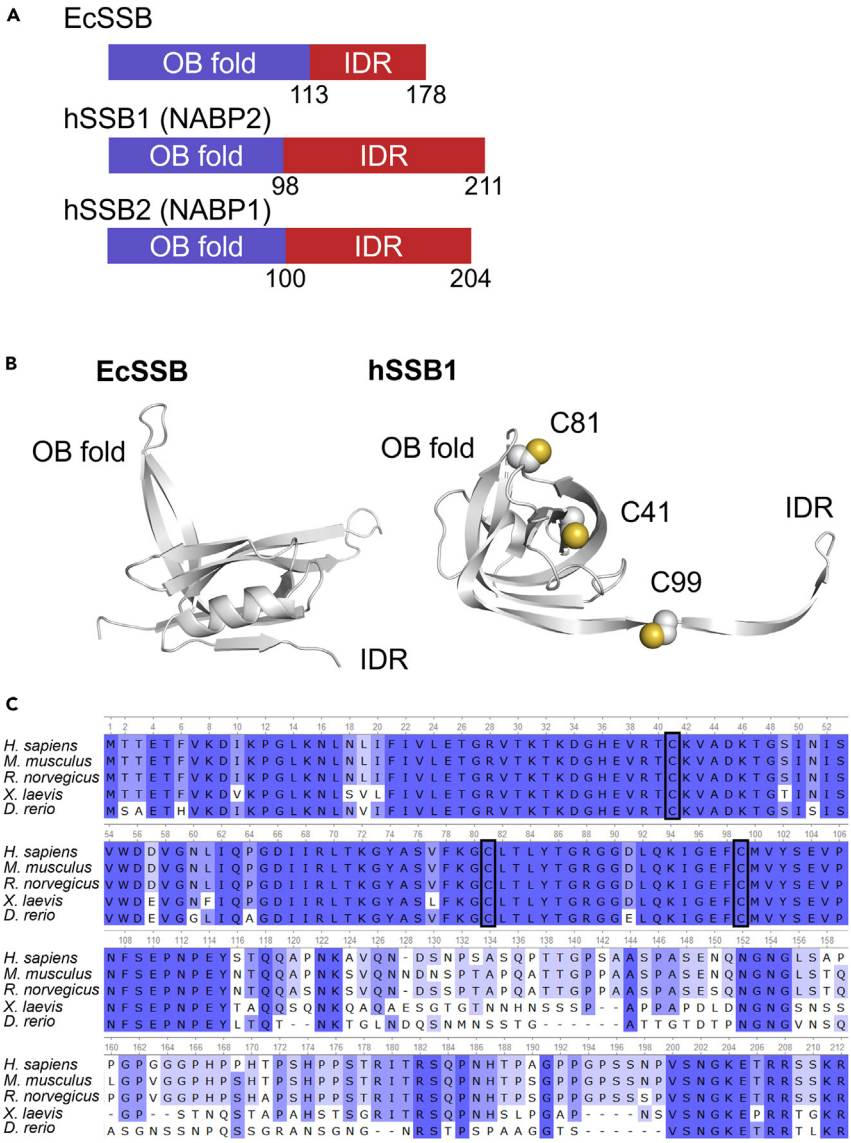

Figure 1. SSB proteins show high structural similarity

(A) Domain structure of *E. coli* (Ec) and human (h) SSB proteins, with amino acid positions indicated at domain boundaries.

(B) Three-dimensional structures of EcSSB (PDB: 4MZ9) and hSSB1 (PDB: 5D8F), with cysteine residues highlighted. (EcSSB contains no cysteines.) Structures shown are visible until aa 114 and 110, respectively.

(C) Amino acid sequence alignment of vertebrate SSB1 orthologs shows high degree of conservation, especially in the OB fold (region 1–115), including the three cysteines (boxed) shown in B.

hOGG1-mediated base excision repair (BER) pathway. hSSB1 relocalizes to chromatin after H_2O_2-induced oxidative stress to recruit hOGG1 to sites of damage and to stimulate its incision activity.[8]

While EcSSB is a stable homotetramer, the ability of hSSB proteins to self-oligomerize appears more dynamic and is of functional significance. Under reducing conditions, hSSB1 was shown to be dominantly monomeric.[6,17] However, unlike EcSSB that lacks cysteines, hSSB1 contains three conserved cysteine residues (at amino acid (aa) positions 41, 81, and 99; Figure 1B) that could potentially facilitate redox-dependent covalent oligomerization via disulfide bonds. Vertebrate SSB1 orthologs show a high degree of sequence conservation, including the presence of all three cysteine residues (Figure 1C). hSSB1 was indeed shown to oligomerize covalently upon oxidative stress, with this feature being abolished by the C99S or C41S substitutions.[17] Based on the observed oligomerization propensity and tetrameric structure of other SSBs, Touma et al. proposed a structural model in which the hSSB1 tetramer is stabilized by C81-C81 and C99-C99 intermolecular disulfide bridges, whereas C41 buried inside the OB fold may act as a redox sensor, with its oxidative status allosterically influencing protein structure.[18] Although the structures of hSSB1 oligomeric forms have not been experimentally clarified, oxidation-dependent hSSB1

oligomerization was found necessary for efficient hOGG1-mediated BER and also for enhanced hSSB1 binding to DNA containing oxidative lesions,[8] but appears dispensable for DSB repair.[17] Furthermore, hSSB1 was observed as a monomer in the ternary SOSS (sensor of ssDNA) complex formed with Integrator complex subunit 3 (INTS3) and SOSS complex subunit C (INIP, C9Orf80, hSSBIP1) proteins.[19,20] hSSB1 directly interacts with INTS3, and the complex plays an essential role in HR-mediated DSB repair via ATM activation, RAD51 recruitment to DNA damage,[20–22] and facilitation of DSB resection by Exo1.[14] Recently, a novel phosphorylation-dependent interaction between MRN and INTS3 in the SOSS1 complex was also shown to facilitate MRN recruitment to DSBs.[23] SOSS1 complex formation is independent of DNA damage, while INTS3 knockdown results in a decrease in nuclear hSSB1 foci after irradiation. INTS3 is required for the transcription of hSSB1; thus, the knockdown phenotype is rescued by ectopic expression of hSSB1.[21] hSSB1 oligomerization proposedly does not interfere with INTS3 interaction.[18] Taken together, these data point to the functional importance of various homo- and heterooligomeric forms of hSSB1 in stress response.

We recently discovered that EcSSB forms liquid-like dynamic condensates under physiological conditions via liquid-liquid phase separation (LLPS).[24] SSB-interacting proteins are selectively enriched inside droplets, while droplet formation is inhibited by ssDNA. Together with earlier data on subcellular distribution of EcSSB,[25] these findings led to a model in which EcSSB condensates serve as organizers of bacterial genome maintenance.[24] Upon genomic stress resulting in exposed ssDNA, droplet contents (EcSSB and partner proteins) can be rapidly deployed at the site of action. In this work we also raised the possibility of hSSB1 (and hSSB2) condensation based on *in silico* predictions.[24]

Here, we show that hSSB1 indeed forms LLPS condensates, with properties that markedly differ from those of bacterial SSB. hSSB1 droplet formation requires coacervation with nucleic acids and is tightly regulated by redox conditions, suggesting the importance of LLPS upon oxidative stress, e.g., in the repair of oxidative DNA lesions and/or in stress-related transcription regulation. Covalent oligomerization is not a prerequisite for hSSB1 LLPS; however, all hSSB1 cysteines are necessary for redox-dependent condensation. We also show that cytoplasmic hSSB1 droplets form in various cancerous and non-cancerous cell lines in response to oxidative stress, colocalizing with stress granules, pointing to unexplored extranuclear stress response roles for hSSB1. These results extend the emerging concept of nucleoprotein LLPS centrally contributing to genome maintenance and other areas of cellular stress response.

RESULTS

hSSB1-ssDNA and hSSB1-ssRNA nucleoprotein coacervates form selectively and reversibly under oxidative conditions

In line with our previous *in silico* predictions,[24] epifluorescence microscopy experiments showed that purified hSSB1 is indeed able to undergo LLPS (Figures 2A, S1, and S2). Importantly, however, unlike in the case of EcSSB, where ssDNA inhibited droplet formation,[24] hSSB1 requires the presence of ssDNA or ssRNA for LLPS. In addition, we found that hSSB1 requires oxidative conditions for robust droplet formation (Figure 2A), in line with the established role of the protein in oxidative DNA damage repair.[8] Hydrogen peroxide (H_2O_2) is a common reactive oxygen species (ROS) *in vivo*,[26] and it is an established agent to mimic oxidative stress conditions both *in vitro* and in cell culture experiments. For reducing conditions, DTT was used. LLPS induction by H_2O_2 was apparent in the presence of either ssDNA or ssRNA; however, ssRNA induced hSSB1 droplet formation to a limited extent even in reducing conditions (Figure 2A). We found that hSSB1 binds ssDNA and ssRNA with similar affinities (Figure 2B; Table S1); thus, the different LLPS propensities of the hSSB1-ssDNA and hSSB1-ssRNA nucleoproteins do not result from differences in the strength of protein-nucleic acid interactions. Liquid-like behavior of hSSB1 condensates is supported by spherical morphology and coalescence of droplets (Figure 2C). In epifluorescence microscopy experiments, condensate formation became apparent at H_2O_2 concentrations in the micromolar range (Figure 2D). Turbidity measurements, which are sensitive to the appearance of small-sized droplets that are yet undetectable in the epifluorescence microscope, indicated phase separation at H_2O_2 concentrations in the low micromolar range, a physiologically relevant regime for cellular oxidative stress[26] (Figures 2E and 2F). Turbidity and microscopy measurements indicated rapid appearance of condensates (<10 min) in response to H_2O_2 treatment, with turbidity eventually decreasing over longer time scales due to droplet fusion and settling, phenomena also seen previously with EcSSB[24] (Figures 2C, 2E, and S3A). Importantly, EcSSB shows LLPS independent of redox conditions, underscoring the unique nature of redox-sensitive LLPS by hSSB1 (Figure S3B). Furthermore, hSSB1 droplet formation was partially reversible upon addition of the reducing agent DTT (Figures S3C and S3D). Prominent droplets disappeared after 1h incubation, leaving only a faint signal on the microscope slide surface. As LLPS systems are generally sensitive to the ionic milieu, we also tested the effect of various salts on hSSB1 LLPS. High, supraphysiological salt concentrations inhibited droplet formation (Figure S4), and addition of KCl at supraphysiological concentration rapidly dissolved droplets after 5 s (Figure S5). Importantly, however, in a quasi-physiological milieu modeling cytoplasmic ionic composition[27] and crowding,[24] hSSB1 exhibited LLPS in the presence of ssDNA in response to H_2O_2 treatment (Figure S4E). Taken together, these findings reflect the propensity of hSSB1 for redox-dependent nucleoprotein coacervate formation under physiological intracellular chemical conditions.

In addition to the factors explored above, the total protein concentration and the protein-DNA stoichiometry could also influence LLPS behavior. Thus, we investigated the dependency of phase separation on hSSB1 and ssDNA concentrations. We found that in the presence of a fixed concentration of ssDNA (2 μM), large phase-separated droplets started to appear when the hSSB1 concentration reached a threshold of 1 μM (hSSB1 monomer concentrations are stated throughout this article) (Figure S6A). Turbidity measurements also confirmed this observation (Figure S6B), and protein concentration-dependent droplet formation was similar in the presence of ssDNA and ssRNA (Figure S6C). Using a fixed amount of hSSB1 we found that the formation of phase-separated droplets showed a bell-shaped dependence on both ssDNA and ssRNA concentration (Figures S6D–S6F).

We also tested the dependence of droplet formation on nucleic acid length (Figure S6G). Longer oligo-dT species showed bell-shaped phase diagrams with maximal turbidity values corresponding to an interaction stoichiometry of around 10–15 nt ssDNA/hSSB1 monomer,

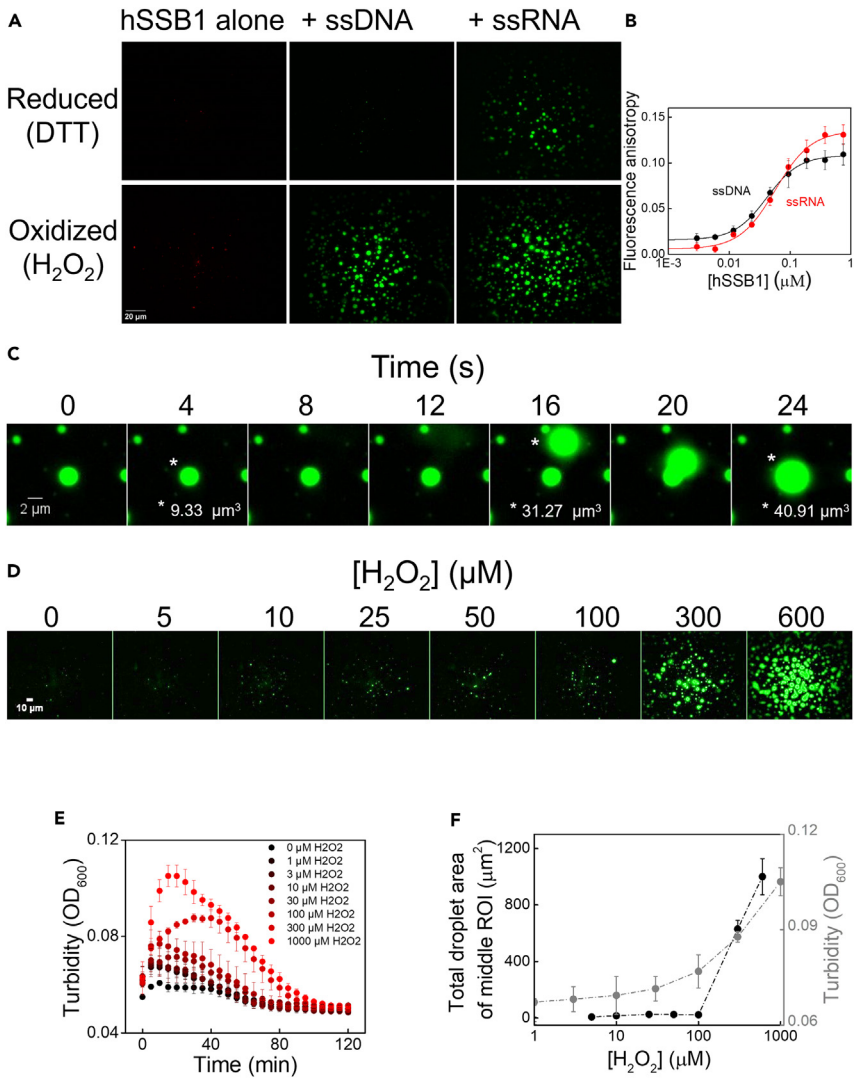

Figure 2. hSSB1 forms ssDNA and ssRNA nucleoprotein coacervates in a redox-dependent manner

(A) ssDNA and ssRNA induce hSSB1 LLPS in oxidative conditions. Representative epifluorescence microscopy images (n = 3 independent measurements) of hSSB1 were obtained in the absence of nucleic acids using labeled hSSB1, or in the presence of labeled ssDNA or ssRNA (cf. Figure S2) in reducing and oxidizing conditions.

(B) ssDNA and ssRNA binding by hSSB1 measured with fluorescence anisotropy titrations. Solid lines show fits using the Hill equation. Means ± SEM are shown for n = 3 independent experiments. Determined equilibrium dissociation constants (K_d) and Hill-coefficients (n) are shown in Table S1.

(C) Droplet coalescence and spherical morphology support liquid-like behavior of hSSB1 droplets. Time-lapse fluorescence images of hSSB1 droplets are shown, recorded in the presence of labeled ssDNA and H_2O_2.

(D) H_2O_2 concentration dependence of the appearance of hSSB1 droplets.

(E) Time-dependent turbidity measurements showing hSSB1 LLPS even at low micromolar H_2O_2 concentrations (2 µM hSSB1, 1 µM dT_{79} ssDNA; H_2O_2 concentrations from bottom to top were 0, 1, 3, 10, 30, 100, 300, and 1000 µM). Error bars represent SEM for n = 3 independent experiments.

(F) H_2O_2 concentration dependence of total droplet area of middle ROIs in microscopy images (panel D) and maximal OD values from panel E. Error bars represent SEM for n = 3 independent measurements.

indicating architectural differences between hSSB1 and EcSSB nucleoproteins, with the latter binding about 35 nt of oligonucleotide by two subunits of a tetramer in LLPS-competent conditions.[24]

The intrinsically disordered region (IDR) is required for strong nucleic acid binding and LLPS

Previously we found that the IDR of EcSSB is essential for LLPS: IDR-truncated EcSSB showed no LLPS propensity and formed amorphous aggregates.[24] In addition, the amino acid composition of the EcSSB IDR has also been shown to be an important determinant of LLPS.[28] Since

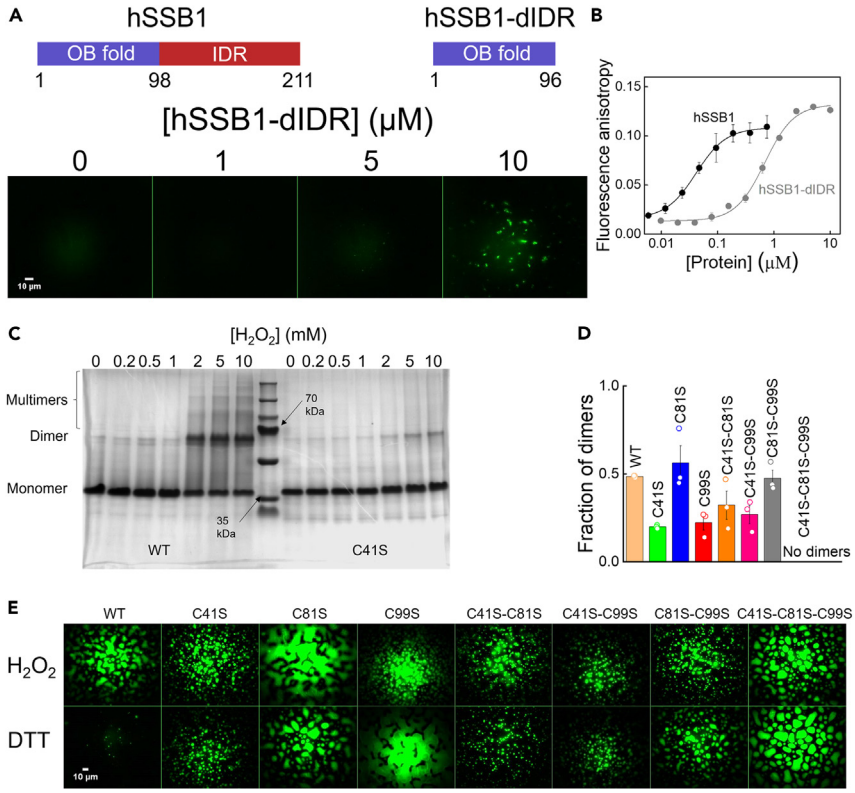

Figure 3. Intrinsically disordered region (IDR) of hSSB1 is indispensable for LLPS propensity, cysteines 41 and 99 mediate covalent oligomerization, while all hSSB1 cysteines are required for redox-sensitive condensation

(A) Domain structure of hSSB1 WT and hSSB1-dIDR constructs (top panel). Epifluorescence images (n = 3 independent measurements) of hSSB1-dIDR in the presence of labeled ssDNA and H_2O_2 show no droplet formation, only amorphous aggregates at high protein concentration (bottom panel).

(B) ssDNA binding of hSSB1 and hSSB1-IDR measured in fluorescence anisotropy titrations show a marked decrease in the ssDNA affinity of hSSB1-dIDR compared to hSSB1 WT. Solid lines show fits using the Hill equation. Means ± SEM are shown for n = 3 independent measurements. Determined equilibrium dissociation constants (K_d) and Hill coefficients (n) are shown in Table S1.

(C) Representative non-reducing SDS-PAGE (n = 3 independent measurements) of WT and C41S hSSB1 variants shows changes in monomer:dimer ratio in response to H_2O_2 treatment. Note that the electrophoretic mobility of monomeric hSSB1 is lower than expected based on its molecular weight of 22 kDa, which is a frequently observed feature for proteins containing long ID regions.

(D) Fraction of dimers formed by hSSB1 variants in response to the highest applied H_2O_2 concentration (10 mM) (cf. Figure S8). Means ± SEM are shown together with individual data points from n = 3 independent measurements.

(E) Epifluorescence microscopy images (n = 3 independent measurements) showing that all hSSB1 variants retained their ability to undergo LLPS, but the redox sensitivity was lost for all non-WT cysteine variants.

hSSB1 also contains a long (113-aa) IDR (Figures 1 and 3A), and our previous *in silico* analysis predicted high LLPS propensity for this region,[24] we tested the LLPS propensity of an hSSB1 variant lacking the IDR region (hSSB1-dIDR). We observed no droplet formation for this construct even in the presence of ssDNA and H_2O_2; only aggregates were observed at higher protein concentrations (Figure 3A). We also found that hSSB1-dIDR shows an about 10-fold decrease in ssDNA binding affinity, compared to the wild-type protein (Figure 3B; Table S1); however, hSSB1-dIDR droplets did not form even at quasi-saturating ssDNA concentrations in the presence of H_2O_2 (Figure S7). These data demonstrate that the IDR has a moderate contribution to ssDNA binding, but is indispensable for phase separation

C41 and C99 are required for redox-dependent covalent oligomerization

A possible mechanism underlying the observed redox-sensitive condensation (Figures 2A and S3A) is covalent oligomerization of hSSB1 through (some of) its three cysteine residues (C41, C81, C99) (Figure 1B), which could increase the multivalency of protein-protein and protein-nucleic acid interactions needed for LLPS.[29,30] C41 was shown to be important for redox-dependent covalent oligomerization, but since it is not exposed to solvent, it was hypothesized to allosterically influence the formation of disulfide bridges between C81 and C99 residues via its oxidative state.[18] To determine the contribution of individual hSSB1 cysteines (Figure 1B) to covalent self-oligomerization and LLPS, we generated all possible Cys-to-Ser substitution variants (C41S, C81S, C99S, C41S-C81S, C41S-C99S, C81S-C99S, and C41S-C81S-C99S). We tested the propensity of hSSB1 variants for covalent oligomerization upon H_2O_2 treatment via SDS-PAGE densitometry (Figures 3C, 3D, and S8). We found that covalent dimers were the major oligomeric species formed upon oxidation, with discernible appearance of

higher-order oligomers in some cases (Figure S8A). Upon H_2O_2 treatment, about half of the total wild type (WT) hSSB1 pool formed dimers at saturating H_2O_2 concentration (Figures 3D and S8B). C41S and C99S variants showed reduced dimer formation, while C81S retained the WT phenotype. For the C41S-C81S and C41S-C99S double substituted variants, we observed similar inhibition of dimerization to that for C41S and C99S. Interestingly, C81S-C99S rescued the WT phenotype, and its initial distribution in the absence of H_2O_2 showed a higher dimer: monomer ratio than that for WT hSSB1, implying that the combined absence of C81 and C99 thiols rendered C41 capable of disulfide formation (Figure S8B). As expected, the triple substituted variant C41S-C81S-C99S showed no covalent oligomerization. We note that all hSSB1 variants, except hSSB1-dIDR, contained a minor non-covalent dimeric species corresponding to 70 kDa (cf. Figures S1 and S8), which was resistant to SDS and DTT treatment, but did not affect the determination of the extent of oxidation-induced hSSB1 covalent oligomerization. Taken together, these data show that both C41 and C99, but not C81, crucially contribute to redox-dependent covalent dimerization.

All cysteines of hSSB1 are required for redox-regulated LLPS propensity

After asserting that the ssDNA binding properties of the above described hSSB1 variants were not affected by the amino acid substitutions (Figure S9A; Table S1), we also investigated the LLPS propensity of these hSSB1 variants (Figure 3E). Interestingly, all constructs retained their ability to undergo LLPS, but the redox sensitivity of this feature was lost in all substituted variants: phase-separated droplets were visible both in the presence of H_2O_2 and in DTT. However, the dependence of droplet formation on the presence of ssDNA was unaffected (Figure S9B). In the presence of ssDNA, C41S and C99S, which were less efficient in covalent oligomerization, and even C41S-C81S-C99S showing no covalent oligomerization, were still able to form phase-separated droplets (Figure 3E).

To ensure that the loss of redox sensitivity is not a result of inhomogeneity in starting materials, we performed LLPS measurements using WT and C41S-C81S-C99S hSSB1 samples reduced overnight with TCEP reducing agent (Figure S10A). We observed the same LLPS propensities as in the earlier experiments. These findings showed that disulfide formation and covalent oligomerization *per se* are not needed for hSSB1 phase separation, but the presence of all cysteines is needed for redox-sensitive behavior.

To test whether H_2O_2 exerts its effect directly through cysteines, we also used the thiol-specific oxidant diamide instead of H_2O_2 (Figure S10B). WT hSSB1 showed similar droplet formation in response to diamide treatment as it did in H_2O_2, highlighting the role of cysteine oxidation as a regulator of redox-sensitive hSSB1 LLPS. The redox-insensitive LLPS behavior of the C41S-C81S-C99S construct was unaffected by diamide treatment.

Genome maintenance proteins are selectively enriched in hSSB1 droplets that act as molecular filters

hSSB1 was shown to promote recruitment of Bloom's syndrome (BLM) helicase to double-stranded DNA breaks during HR.[15] In addition, integrator subunit 3 (INTS3) is required for the transcription of hSSB1[21] and serves as a major interacting partner of hSSB1 (and hSSB2) in the ternary SOSS complex, which is crucial for DSB repair[20–22] (Figure 4A). Furthermore, hSSB1 was shown to assist the repair of ROS-induced DNA damage by recruiting hOGG1 to chromatin.[8] Our fluorescence microscopy experiments showed that the mentioned proteins, and also hSSB2, were readily enriched inside LLPS droplets formed by hSSB1 (Figures 4B and 4C). The SOSS component INIP, which only forms interactions with INTS3 but not with hSSB1,[20] showed enhanced enrichment in hSSB1 droplets in the presence of INTS3 (Figures 4B and 4C). To confirm the necessity of specific interactions with hSSB1 for enrichment in hSSB1 condensates, we identified that neither the protein EGFP nor the small molecule fluorescein become enriched in condensates (Figures 4B and 4C), indicating strong regulation regarding the contents of hSSB1 LLPS droplets. To rule out that other proteins are enriched inside hSSB1 droplets solely due to disulfide crosslinking resulting from the applied oxidizing conditions, we tested whether genome maintenance proteins can be enriched in the droplets formed by the C41S-C81S-C99S variant hSSB1 protein (Figure S11A). We observed similar coacervation to that seen with WT hSSB1. Furthermore, we tested whether the presence of ssRNA instead of ssDNA in hSSB1 droplets influences the enrichment of interaction partners, thus contributing to selectivity, but we found no such difference (Figure S11B). These data show that hSSB1 condensates exert molecular filter functions by selectively recruiting and retaining interaction partners, similar to what we observed for the EcSSB protein.[24]

Oxidative stress induces hSSB1 organization into cytoplasmic foci that colocalize with stress granules but not with P-bodies

After our *in vitro* observation of redox-sensitive LLPS by hSSB1 in the presence of either ssDNA or ssRNA, we sought to explore the possibility of intracellular condensation of endogenous hSSB1 in HeLa cells under oxidative stress. hSSB1 has previously been implicated in nuclear functions, mostly by immunofluorescence of pre-extracted cells that remove the soluble protein fraction prior to fixation.[5,8,13,15,17,21,22] Here, without pre-extraction, we detected hSSB1 throughout the cell, both in the nucleus and cytoplasm, with the exception of the nucleolus (Figure 5A). In untreated cells, the majority of hSSB1 is found in the nucleus, but a discernible fraction is located in the cytoplasm (Figure 5A). Under these conditions, the cytoplasmic hSSB1 fraction showed disperse distribution with no apparent local enrichment or condensation. Surprisingly, we detected a significant, dose-dependent decrease in nuclear hSSB1 fluorescence intensity upon H_2O_2 treatment (Figure 5B). Moreover, we observed that upon acute oxidative stress caused by H_2O_2 treatment, endogenous hSSB1 became organized in multiple dense cytoplasmic foci in the size range of <1 μm (Figure 5A). Our *in vitro* measurements confirmed the ability of the applied antibodies to enter and stain hSSB1 droplets, thus enabling immunostaining of hSSB1 under LLPS conditions (Figure S12). Stress granules (SGs) have been identified as cytoplasmic, membraneless ribonucleoprotein granules that form upon rapid changes in intra- or extracellular conditions, including oxidative stress.[31,32] SGs exhibit liquid-like properties and were implicated in fine-tuning protein expression to adapt to changed environments. Ras GTPase-activating protein-binding protein 1 (G3BP1) was shown to be a major factor for SG assembly[33]; therefore, we used G3BP1 staining to visualize SGs and assess their colocalization with hSSB1 granules. Diffuse G3BP1 staining with no SG formation was observed in

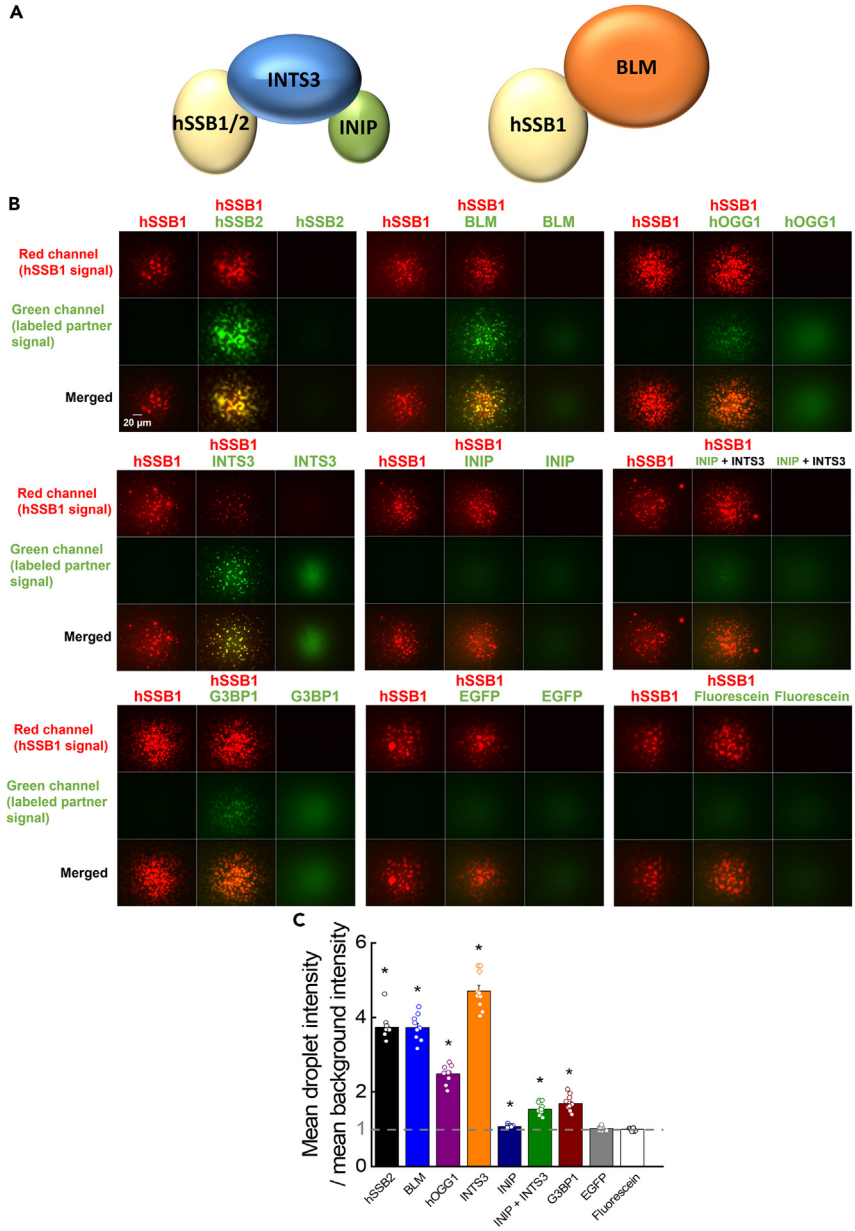

Figure 4. Genome maintenance proteins are selectively enriched inside hSSB1 droplets, reflecting interaction-based control of their content

(A) Schematic illustration of SOSS and hSSB1-BLM helicase complexes. INTS3 interacts both with INIP and hSSB1, while there is no direct interaction between INIP and hSSB1. hSSB2 can replace hSSB1 in the SOSS complex.

(B) Two-channel fluorescence microscopy images ($n = 3$ independent measurements) showing enrichment of proteins inside hSSB1 droplets. Columns represent three separate experiments (hSSB1, hSSB1 + partner, partner alone), while rows represent fluorescence channels. Labeled hSSB1 and/or labeled interaction partner were present in the samples, together with ssDNA and H_2O_2. In experiments containing labeled INTS3, for technical reasons, labeled ssDNA was used to visualize unlabeled hSSB1 droplets. See STAR Methods for further details. Red channel shows hSSB1 droplets, green channel shows labeled interaction partners. Yellow color indicates co-condensation. Images were not background corrected.

(C) Enrichment of various components in hSSB1 droplets, calculated as the ratio of the mean signal intensity of the partner within droplets and the mean background intensity, determined from images shown in panel B. A molecule is enriched inside hSSB1 droplets if the ratio is higher than unity. Means ± SEM are shown together with individual data points of 10 images from $n = 3$ independent measurements. Asterisks (*) indicate significant difference from unity ($p < 0.01$, 2-tailed t-test).

untreated cells (Figure 5A). However, we were able to trigger SG formation upon acute H_2O_2-induced oxidative stress (Figures S13A and S13B) and observed strong colocalization between cytoplasmic hSSB1 granules and SGs (Figures 5C and 5D). Manders' split coefficients for the fraction of G3BP1 overlapping with hSSB1 indicated robust colocalization. However, Manders' coefficients for the fraction of hSSB1

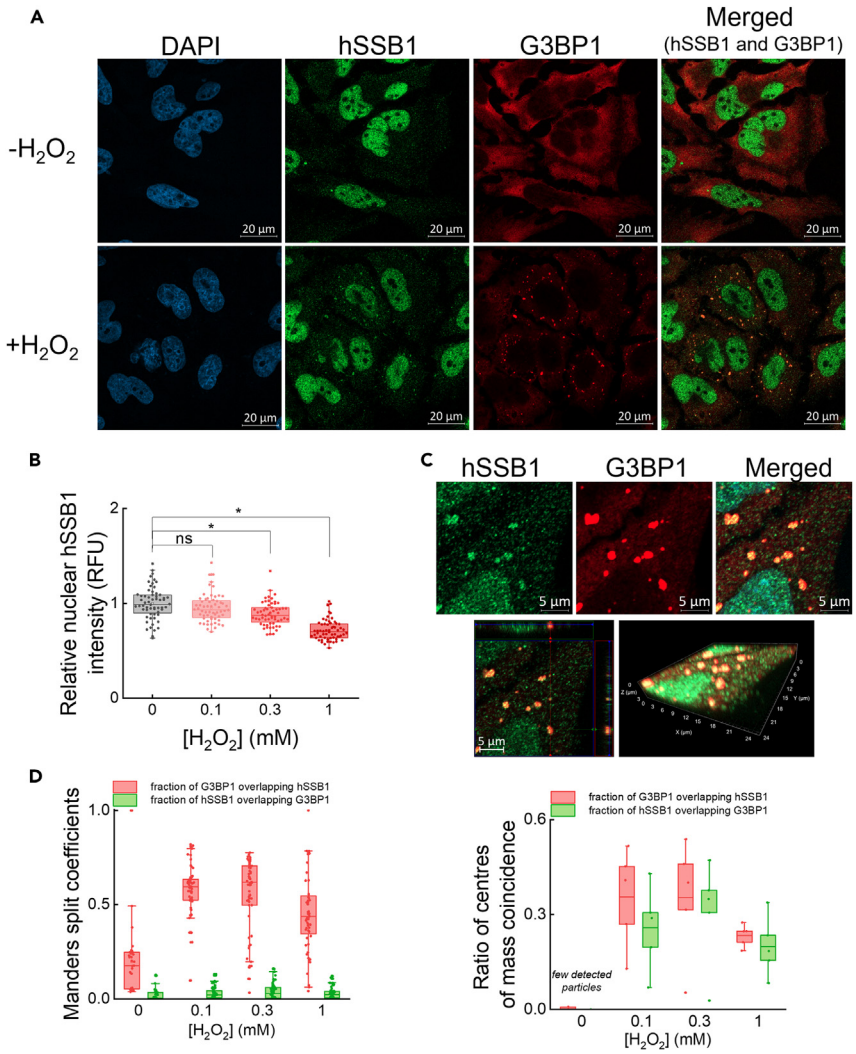

Figure 5. hSSB1 is organized into cytoplasmic foci upon oxidative stress, colocalizing with stress granules

(A) Representative confocal microscopy images (n = 3 independent experiments) of immunostained, untreated or H_2O_2-treated (300 µM, 2 h) HeLa cells. Blue channel shows nuclear DAPI stain, green and red channels show endogenous hSSB1 and G3BP1 stress granule marker, respectively. Merge image was created from hSSB1 and G3BP1 channels; yellow cytoplasmic foci indicate enrichment of hSSB1 in G3BP1-positive SGs.

(B) Relative nuclear hSSB1 intensity decreases upon H_2O_2 treatment (Mann-Whitney-test; * indicates significance; 'ns', not significant; $p < 0.05$; RFU, relative fluorescence units). Dots indicate individual nuclear intensities.

(C) Top row, magnified confocal images of a H_2O_2-treated HeLa cell (cf. panel A), with hSSB1 and G3BP1 showing colocalized enrichment in cytoplasmic stress granules. Bottom row, 3D reconstructed images of the same ROI from confocal z stack images (16 slices, 3.6 µm optical sectioning). Green and red channels show endogenous hSSB1 and G3BP1 stress granule marker, respectively; yellow color indicates colocalization.

(D) Manders' split coefficients (left) and object based colocalization (right) of detected cytoplasmic hSSB1 and G3BP1 condensates. Dots indicate individual data derived from an image.

overlapping with G3BP1 appeared to be lower. This resulted from different levels of enrichment of G3BP1 and hSSB1 in SGs compared to the rest of the cytoplasmic intensity. Nevertheless, SG-independent hSSB1 granulation was scarcely seen, also supported by the ratio of object based colocalization of droplets (Figure 5D). Furthermore, similar to the tested genome maintenance proteins, recombinant G3BP1 was also able to enrich inside hSSB1 droplets *in vitro*, in the presence of either ssRNA or ssDNA, unaffected by Cys-to-Ser mutations in hSSB1 (Figures 4B, 4C, and S11). Based on these findings, we conclude that hSSB1 is enriched inside SGs and colocalizes with the G3BP1 SG marker.

Paquet et al. demonstrated that hSSB1 robustly oligomerizes in U2OS cells upon oxidative stress.[17] Therefore, we examined the extent of cellular hSSB1 covalent oligomerization at H_2O_2 concentrations that led to foci formation in HeLa cells (Figures S13C and S13D). Upon H_2O_2 treatment, we observed a modest but significant increase in the dimer/monomer ratio of hSSB1 in whole cell lysates,[17] which aligns well with our observation that a discernible but small fraction of the total cellular hSSB1 pool localizes to SGs in HeLa cells (Figure 5A). As we

demonstrate that covalent oligomerization *per se* is neither a prerequisite for LLPS, nor is it alone sufficient for redox-dependent condensation (Figure 3), we propose that in the cellular context, redox-dependent hSSB1 condensation may either be triggered by a small oxidized, but not necessary covalently linked fraction of hSSB1 oligomers, or be controlled by additional factors to be identified in further studies.

We also assessed hSSB1 subcellular patterns by transiently overexpressing EGFP-fused hSSB1 (hSSB1-EGFP) in HeLa cells. Cells overexpressing hSSB1-EGFP showed granulation of both hSSB1-EGFP and G3BP1 even in the absence of oxidative stress, which was not seen in non-transfected cells (Figure S14A, cf; Figure 5A). Therefore, we investigated whether overexpression of hSSB1-EGFP, or that of EGFP alone, can influence SG formation. Assessed as a function of H_2O_2 concentration, we found the fraction of SG-containing cells to be similar in both EGFP- and hSSB1-EGFP expressing cells, with hSSB1-EGFP foci colocalizing with G3BP1 (Figures S14B and S14C). While indicating that the transfection procedure and/or EGFP expression *per se* induce SG formation, in line with recent results suggesting that EGFP expression causes oxidative stress,[34] these experiments corroborated the inclusion of hSSB1 in stress granules.

Processing-bodies (P-bodies) are membraneless ribonucleoprotein compartments associated with RNA degradation processes and share a number of components with SGs.[35,36] We used co-staining of P-body marker SK1-Hedls[37] and hSSB1 to investigate whether hSSB1 droplets colocalize with P-bodies under normal and oxidative stress conditions (Figure S15). We observed no colocalization, therefore we concluded that hSSB1 is not included in P-bodies.

Stress granule associated hSSB1 condensation is accompanied by a decrease in nuclear hSSB1 levels in various cell lines in response to various forms of cellular stress

It has been reported that hSSB1 relocalizes to chromatin after acute oxidative stress.[8] Our experiments aimed to observe cytoplasmic granulation showed no nuclear enrichment, but a significant decrease in nuclear hSSB1 signal after 2 h of H_2O_2 treatment (Figures 5A and 5B). Since nuclear accumulation was previously observed after 0.5 h of H_2O_2 treatment,[8] we investigated the time dependence of cytoplasmic hSSB1 granulation and nuclear enrichment (Figure S16A). Intriguingly, we found that 0.5 h of H_2O_2 treatment indeed causes a significant increase in nuclear hSSB1 intensity levels, but after 2 h the nuclear fraction significantly decreased compared to control (Figure S16B). Conversely, stress granule formation accompanied by cytoplasmic hSSB1 condensation became robust after 2 h (Figure S16C). Manders' colocalization between G3BP1 and hSSB1 also appeared higher after 2 h of H_2O_2 treatment (Figure S16D). Since the mentioned experiments were carried out in serum-free media, we tested whether acute serum deprivation causes similar phenotypes (Figure S17A). We observed no cytoplasmic granulation, but a time-dependent decrease in nuclear hSSB1 fraction, which was restored after 4 h of serum deprivation (Figure S17B). Based on our results, we conclude that oxidative stress causes rapid accumulation of hSSB1 in nuclei, which is then depleted concomitantly with cytoplasmic accumulation. Other nuclear phenotypic changes, such as condensation similar to that seen in the cytoplasm, were not observed upon oxidative stress or serum deprivation. Small dense hSSB1 foci were discernible in nuclei (e.g., Figure S16A, green channel), but these were permanently present and did not respond to any applied treatment reported in the present work.

Next, we aimed to investigate whether oxidative stress induced, SG-associated hSSB1 granulation can also be observed in other cell lines. Besides HeLa, we treated HEK293T and HFF-1 cells with H_2O_2 (Figure S18A). In each case we observed a significant decrease in nuclear hSSB1 intensity after 2 h of treatment (Figure S18B), accompanied by a significant increase in the number of hSSB1-associated SGs per cell (Figures S18C and S18D), indicating that oxidative stress causes transient nuclear hSSB1 depletion and gradual, SG-associated hSSB1 condensation in both cancerous and non-cancerous cell lines, suggesting that redox-dependent hSSB1 LLPS can occur in cells with different metabolic profiles.

Subsequently, we investigated the effect of a variety of cellular stressors on hSSB1 condensation (Figure 6A). Besides H_2O_2, we treated HeLa cells with potassium bromate ($KBrO_3$) and sodium arsenite ($NaAsO_2$), which are often used to induce direct oxidative stress.[17,33] Menadione was shown to generate ROS through redox cycling while disrupting mitochondrial membrane potential, triggering cytochrome *c* redistribution to the cytosol, thus inducing indirect, internal oxidative stress.[38] DTT was used to induce endoplasmic reticulum stress by inhibiting protein folding through the reduction of disulfide bridges.[39] DTT is also responsible for ROS production by influencing cell signaling and the glutathione system.[39] Treatment with $NaAsO_2$, menadione sodium bisulfite, and DTT, similarly to H_2O_2, resulted in the decrease of nuclear hSSB1 signal compared to appropriate serum deprivation controls according to treatment time (Figure 6B), accompanied by SG associated hSSB1 granulation (Figures 6C and 6D). These stressors exert their effect mainly in the cytoplasm, thus we wished to investigate an agent that is genotoxic and disrupts DNA metabolism. Etoposide inhibits DNA topoisomerase II, thus leading to the accumulation of DNA breaks, at which hSSB1 was shown to localize.[13,15,40] Unexpectedly, no nuclear hSSB1 accumulation or condensation was observed in response to etoposide treatment. Nevertheless, taken together our data show that various stress agents affecting redox conditions, protein folding, and ROS signaling induce cytoplasmic, SG associated granulation of hSSB1.

hSSB1 silencing enhances stress granule formation upon oxidative stress

After establishing that hSSB1 shows SG-associated cytoplasmic condensation during cellular stress response, we set out to examine the effect of hSSB1 silencing (Figure S19A) on SG formation. Confocal images of immunostained HeLa cells showed robust decrease in nuclear hSSB1 intensity upon silencing (Figure S19B). Upon oxidative stress, SGs were visible in the cytoplasm even when hSSB1 was silenced. Moreover, the residual hSSB1 fraction still showed discernible enrichment inside G3BP1-stained SGs (Figure S19B). In hSSB1-silenced cells, nuclear hSSB1 intensity was around 3-fold lower compared to control cells, but the oxidative stress-induced nuclear depletion remained unchanged (Figure S19C). Surprisingly, hSSB1 silencing resulted in a significantly higher fraction of SG + cells after 0.3 mM H_2O_2 treatment, compared to non-silenced controls (Figure S19D). This result suggests that hSSB1 may play a stress dose dependent regulatory role in SG formation.

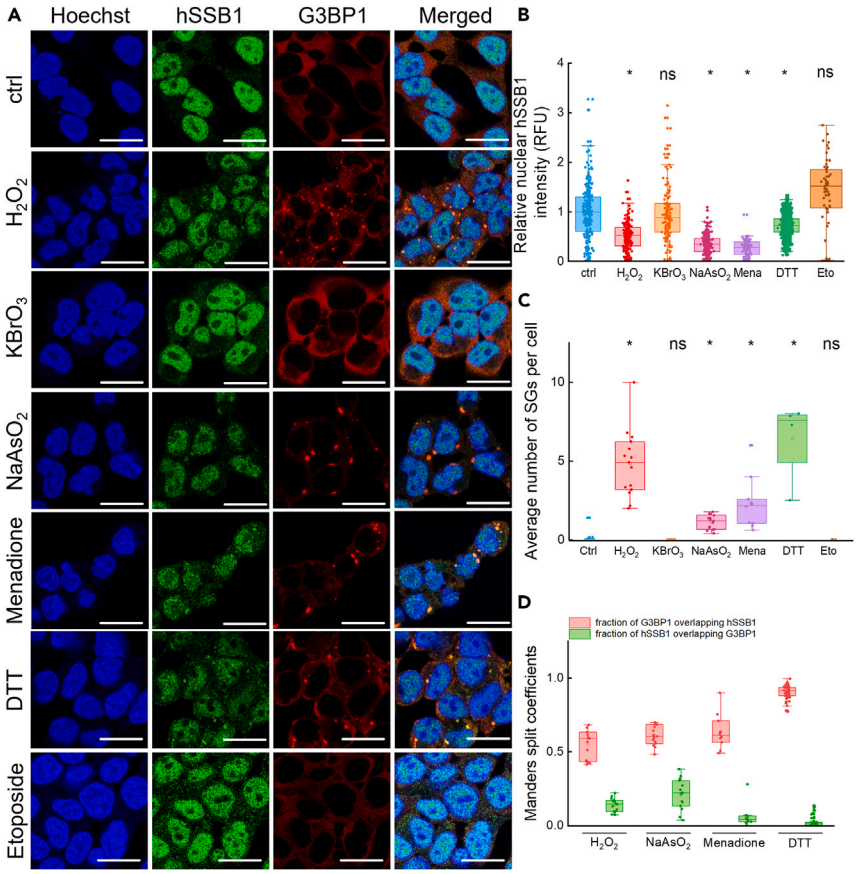

Figure 6. hSSB1 is enriched in stress granules in response to various cellular stressors

(A) Representative confocal microscopic images (n = 3 independent experiments) of immunostained HeLa cells treated with various stress agents (H_2O_2: 1 mM, 2 h; $KBrO_3$: 30 mM, 2 h; $NaAsO_2$: 0.5 mM, 2 h; Menadione sodium bisulfite: 100 μM, 4 h; DTT: 1 mM, 2 h; Etoposide: 100 μM, 2 h). Blue channel shows nuclear Hoechst stain; green and red channels show endogenous hSSB1 and G3BP1 stress granule marker, respectively. Merged image was created from all three channels; yellow cytoplasmic foci indicate enrichment of hSSB1 in G3BP1-positive SGs. Scale bar: 20 μm.

(B) Besides H_2O_2, $NaAsO_2$, menadione sodium bisulfite (mena), and DTT triggered a decrease in nuclear hSSB1 intensity, while $KBrO_3$ and etoposide (eto) did not. Changes in nuclear hSSB1 intensities (RFU, relative fluorescence units) were normalized to appropriate serum deprivation controls. Dots indicate individual nuclear intensities (Kruskal-Wallis test with Dunn's post-hoc test, * indicates significant difference, 'ns' not significant, $p < 0.05$).

(C) Besides H_2O_2, $NaAsO_2$, menadione sodium bisulfite, and DTT induced robust SG formation, while $KBrO_3$ and etoposide did not. Changes in the average number of SGs per cell are shown. Dots represent average SG numbers derived from individual images (Kruskal-Wallis test with Dunn's post-hoc test, * indicates significant difference, $p < 0.05$).

(D) Manders' split coefficients show colocalization of hSSB1 and G3BP1 condensates upon treatment with H_2O_2, $NaAsO_2$, menadione sodium bisulfite, and DTT. Dots represent Manders' coefficients derived from individual images.

DISCUSSION

In this work, we show that hSSB1 forms phase-separated liquid condensates under physiologically relevant macromolecular and ionic conditions *in vitro* and shows cytoplasmic, SG-associated granulation upon various forms of cellular stress in both cancerous and non-cancerous cell lines. hSSB1 coacervates with both DNA and RNA, in a stoichiometry-dependent fashion, with its condensation being selectively initiated by oxidative conditions (Figures 2 and S3–S6). hSSB1 condensation is effective even at low protein concentrations, without the need for molecular crowders (Figures S6A–S6C) and is driven by hSSB1's intrinsically disordered region (IDR) (Figures 3A and S7), in line with PDB-deposited crystal structures obtained with a truncated hSSB1 construct supporting the propensity for IDR-IDR intermolecular interactions (PDB: 5D8E, 5D8F, no accompanying publication) (Figure 7A).

Importantly, the dependence of hSSB1 LLPS on oxidative conditions (Figures 2 and S3) strongly suggests a cellular oxidative stress sensing/response role for the protein. Effects caused by ROS are thought to be exerted locally,[41,42] where hSSB1 droplets, as first responders, could rapidly form on exposed single-stranded nucleic acid segments.

We also show that other genome maintenance proteins interacting with hSSB1 can readily and selectively be enriched in hSSB1 droplets (Figures 4 and S11). hSSB1 condensates can thus recruit required factors to the site of action, and also act as a molecular filter to restrict the

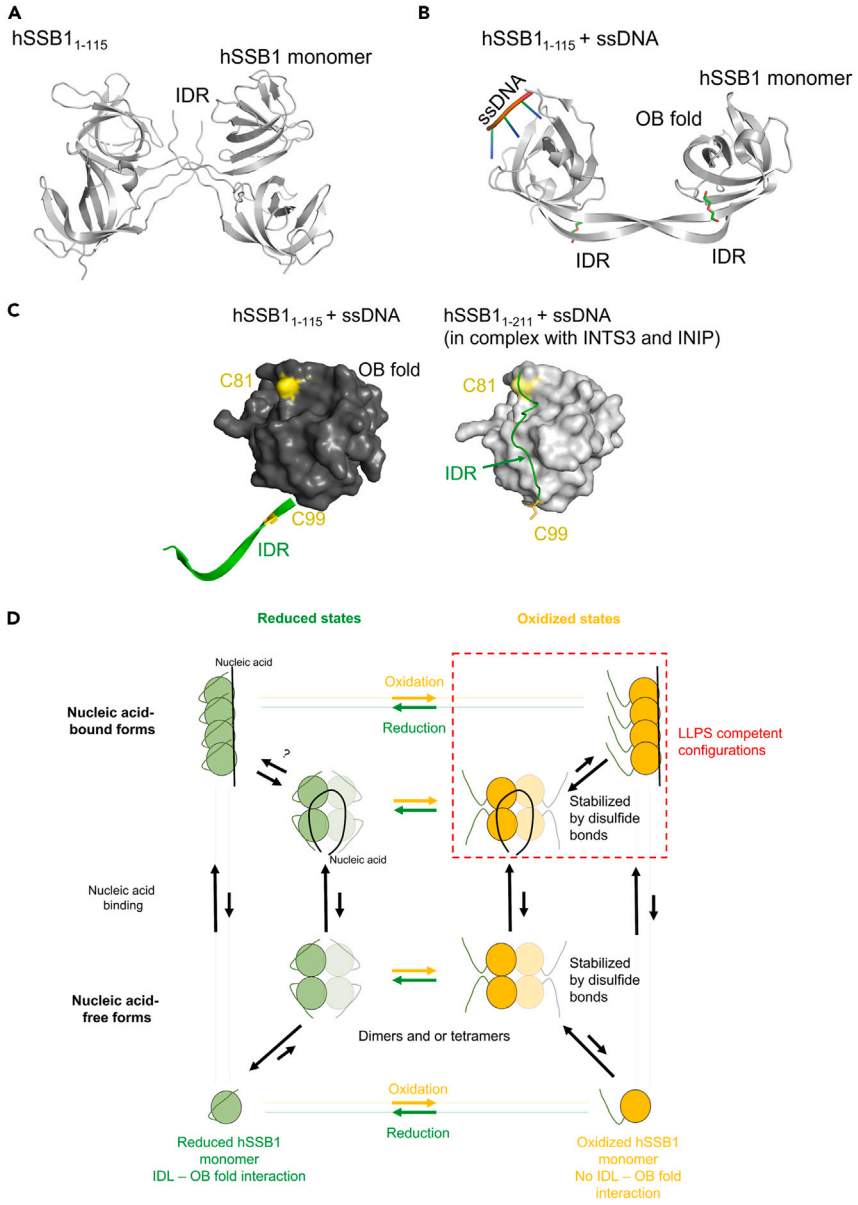

Figure 7. Proposed model for the role of hSSB1 IDR tail flexibility in redox-dependent LLPS regulation

(A and B) Crystal structures of a truncated hSSB1 construct (amino acids 1–115) lacking the majority of the IDR, in the absence (A) and presence of ssDNA (B) (PDB: 5D8E, 5D8F, respectively). In both conditions, interactions can be observed between the N-terminal IDR segments contained in the constructs.

(C) Comparison of the structure of ssDNA-bound truncated hSSB1 (dark gray, PDB: 5D8F, cf. panel B) and that of full-length hSSB1 in the ssDNA-bound SOSS1 complex (light gray, PDB: 4OWW; INTS3 and INIP structures were removed for clarity).[19] The N-terminal part of the IDR is not resolved in the latter structure. OB domain is shown as a surface model and the IDR tails are represented as green cartoons. Note the large difference between IDR conformations.

(D) Proposed model for regulation of hSSB1 LLPS. In the reduced form and in the absence of nucleic acids, hSSB1 is in a dynamic equilibrium between monomeric and oligomeric states, with the monomeric form being favored.[6,17] Binding to single-stranded nucleic acids may either stabilize/facilitate protein oligomerization, or hSSB1 monomers can bind independently to the nucleic acid lattice in a sequential order without oligomerization. Under reducing conditions, the C-terminal part of the hSSB1 IDR can interact with the OB fold (cf. panel C, right side) both in the absence and presence of nucleic acids. Upon oxidation, the IDR is released from the OB fold and participates in intermolecular IDR-IDR interactions (cf. panel C, left side). Covalent hSSB1 oligomers form via disulfide bridges involving C41 and C99; however, covalent oligomerization is not required for LLPS *per se* (cf. Figures 3D and 3E). LLPS is triggered by multivalency brought about by nucleic acid binding (independent of hSSB1 oligomerization state) and oxidation-dependent, conformationally regulated IDR-IDR interactions.

localization of other proteins. One such example may be BER where hSSB1 was shown to recruit hOGG1 to chromatin.[8] However, considering that we observed hSSB1-driven LLPS also in conjunction with ssRNA (Figure 2A), the roles of hSSB1 LLPS may not be limited to genome repair, as it may also be effective in RNA metabolic processes both in the nucleus and in the cytoplasm (see below).

While intermolecular IDR-IDR interactions appear to be a major driving force for LLPS (Figure 3A), binding of single-stranded nucleic acids is also crucial for coacervation (Figures 2A and S6D). hSSB1 was shown to exist dominantly as a monomer in the absence of nucleic acids.[6,17] However, as LLPS processes generally require multivalent interactions, we propose that single-stranded nucleic acids can either act as a scaffold to which multiple hSSB1 monomers can bind sequentially and independently or as a stabilizer for oligomerization. In either case, the multivalency of SSB-SSB interactions is enhanced in addition to the increased local concentration of SSB IDR regions. The bell-shaped ssDNA concentration dependence of hSSB1 LLPS (Figures S6D–S6G) can be explained based on this model, regardless of the oligomerization state of the protein. When the concentration of ssDNA molecules exceeds the SSB binding stoichiometry, the probability of multiple SSB molecules binding to the same ssDNA molecule decreases, leading to a lower LLPS propensity. However, our findings that despite significant hSSB1 oligomerization upon oxidation in the absence of nucleic acids (Figures 3C and 3D), LLPS is only observed upon nucleic acid binding, indicate additional unexplored roles for nucleic acid binding, potentially distinct from the scaffolding function.

The role of protein oxidation in LLPS regulation is especially intriguing. According to an emerging concept, cysteine residues within proteins may act as regulatory switches in redox signaling.[43,44] In this work we comprehensively assessed the roles of each of hSSB1's cysteine residues in the interplay between covalent oligomerization and nucleoprotein condensation (Figures 3C–3E, S8, and S9). On one hand, we show that covalent oligomerization of hSSB1, mediated by residues C41 and C99, is not a prerequisite for forming LLPS condensates (Figure 3D). On the other hand, the capability for covalent oligomerization alone is not sufficient for redox-dependent LLPS, for which all three hSSB1 cysteines are required (Figure 3E). Taken together, our observations point toward a delicate autoregulatory mechanism for LLPS, which apparently involves oxidation-dependent hSSB1 structural changes. While the structure of oxidized hSSB1 is yet unknown, existing crystal structures also support a regulation model as follows. In both of nucleic acid-free and ssDNA-bound structures of a truncated hSSB1 construct lacking the majority of the IDR (PDB: 5D8E, 5D8F), extensive interactions between the remaining parts of the IDR are observed (Figures 7A and 7B). In contrast, in the SOSS1 (INTS3, INIP, SSB1) complex, the same region of full-length hSSB1 folds back onto the OB domain both in the presence and absence of ssDNA.[19] Moreover, the C-terminal part of the IDR is not resolved, probably because it is disordered (Figure 7C). The large difference in protein structure, i.e., the position of the IDR tail, in the above-mentioned structures highlights the mobility of the tail and its capability to either bind to the OB fold intramolecularly or to interact with other hSSB1 tails (Figure 7C). Importantly, in the OB domain-bound form of the IDR, its resolved C-terminal part lies in a valley on the OB domain's surface, which includes cysteine 81 and a hydrophobic pocket adjacent to C99 (Figure 7C). Based on these observations, we can envision a scenario in which the oxidation of these residues (C81, C99), and also that of cysteine 41, could potentially alter the structure of hSSB1 and significantly weaken the interaction between the IDR and the OB fold. This effect may facilitate intermolecular IDR-IDR interactions that are essential for LLPS. The observed IDR-IDR and IDR-OB interactions are apparently mutually exclusive as they involve the same residues and likely compete with each other based on the structural data.

Our results suggest that all three cysteines in their reduced form contribute to the inhibition of interprotein interactions essential for LLPS, regardless of the presence of nucleic acids, possibly by facilitating IDR-OB fold interactions and thus inhibiting IDR-IDR interactions. Single or combinatorial mutations of any of the cysteines eliminate the inhibitory effect and thus abolish redox sensitivity of hSSB1 LLPS (Figure 3E). In addition, cysteines 99 and 41 are involved in the formation of covalently bound oligomers. While covalent oligomers are not required for hSSB1 LLPS, they were shown to bind ssDNA with enhanced affinity compared to the monomeric form, indicating a role in regulating interactions within and stability of the nucleoprotein complex.[45] In addition, disulfide bridges may stabilize the IDR in an OB-unbound form in hSSB1 oligomers. Based on the above findings, we propose a model for a regulatory mechanism that ensures that robust LLPS is only triggered when the hSSB1 protein is oxidized and bound to nucleic acids (Figure 7D). Although redox-dependent regulatory modifications[44] are being identified in an increasing number of proteins,[46] evidence is still scarce for redox-sensitive amino acid modifications governing LLPS propensity.[47,48] Further exploration of redox-dependent molecular changes in hSSB1 nucleoprotein coacervates will likely yield key insights into mechanisms of oxidative stress response.

As hSSB1 and hSSB2 show high structural resemblance (Figure 1A), recently we also investigated the LLPS propensity of hSSB2 *in vitro*.[49] Similar to hSSB1, hSSB2 also undergoes LLPS upon ssDNA binding in physiologically relevant conditions, mediated by the IDR region. Interaction partners of hSSB2 become selectively enriched inside hSSB2 condensates. However, *bona fide* hSSB2 condensation was only seen in reducing conditions, while oxidation promoted the formation of branched, solid-like nucleoprotein particles. All cysteine residues are conserved between hSSB1 and hSSB2 (C45, C85, C103 in hSSB2); thus, the observed differences between hSSB1 and hSSB2 condensation indicate additional, yet unknown structural mechanisms of redox-sensitive LLPS regulation besides cysteine oxidation.

In the present study we found that a discernible fraction of the hSSB1 protein is present in the cytoplasm, which is organized into distinct granules upon acute oxidative stress (Figures 5A and 5B), although this far only nuclear functions have been described for hSSB1. Cytoplasmic hSSB1 foci colocalize with stress granules (Figures 5C and 5D) but not with P-bodies (Figure S15). Interestingly, hSSB1 has not been implicated to be me a member of the SG proteome by previous approaches aiming to identify SG constituents.[50]

The previously reported increased H_2O_2 sensitivity of cells upon hSSB1 silencing was interpreted as a result of the defect in BER.[8] However, our current findings suggest that hSSB1 plays additional roles in processes distinct from genome repair. We find that hSSB1 forms coacervates with ssRNA as effectively as with ssDNA (Figure 2A). Thus, ssDNA regions appearing upon DNA damage can act as a scaffold to initiate hSSB1-driven LLPS in the nucleus, while in the cytoplasm ssRNA regions can facilitate droplet formation and incorporation of hSSB1 condensates into SGs. hSSB1 knockdown resulted in an elevation in the fraction of cells displaying SGs upon sublethal H_2O_2 treatment (Figure S19D),

indicating a negative influence of hSSB1 on SG formation. Interestingly, hSSB1 is not the only genome maintenance protein that has been shown to enter SGs. BLM helicase and hOGG1, interaction partners of hSSB1,[8,15] which we demonstrate to be enriched in hSSB1 granules *in vitro* (Figure 4), were detected in SGs formed upon various forms of stress.[51,52] BLM was found to inhibit SG formation via unwinding cytoplasmic RNA G-quadruplexes associated with cellular stress response. BLM knockdown resulted in increased SG formation, similarly to hSSB1 knockdown in our study. Considering that hSBB1 is needed for stability and recruitment of BLM at DNA double-strand breaks and stalled replication forks,[15] one can envision a similar scenario whereby hSSB1 could assist the recruitment of BLM to RNA quadruplexes inside SGs, further expanding the physiological implications of our results. Similarly, hSSB1 may facilitate the recruitment of hOGG1 to SGs.

We found that oxidative stress induced rapid nuclear accumulation of hSSB1, followed by cytoplasmic accumulation (Figure S16B). Besides this effect, we did not detect redox-regulated nuclear hSSB1 condensation. As hSSB1 oligomerization is required for efficient hOGG1-mediated BER[8] and we demonstrated that hOGG1 is readily enriched inside hSSB1 condensates (Figure 4), redox-dependent LLPS may play a role in the repair of oxidative DNA lesions. Recent evidence also suggests that hSSB1's LLPS propensity may be modulated by interaction partners. INTS3 is a major nuclear interacting partner of hSSB1 in the SOSS1 complex,[21,53] and it also contains a C-terminal IDR.[54] The ternary SOSS1 complex was recently demonstrated to undergo LLPS, with condensates being localized to laser induced DSBs.[54] The purified SOSS1 complex was able to undergo LLPS in the presence of molecular crowder, and droplet formation was enhanced upon addition of ssRNA or ssDNA. Truncation of the C-terminal IDR of INTS3 inhibited droplet formation by the SOSS1 complex *in vitro*. While the redox dependence of SOSS1 LLPS has not been tested, these findings indicate that the LLPS properties of hSSB1 are significantly modulated by its partners in the SOSS1 complex. LLPS by SOSS1 was also recently demonstrated to be involved in transcription regulation and the prevention of R-loop induced genome instability.[55] Nuclear hSSB1 puncta were seen even in stress-free conditions, which resembled the small nuclear hSSB1 foci visible in our experiments both under stress-free and stress conditions (e.g., Figure S16A, green channel). Taken together, these findings bear further implications for the physiological importance of hSSB1-driven nuclear LLPS transitions.

Besides hSSB1 and the SOSS1 complex, the well-known ssDNA-binding protein RPA has also recently been shown to undergo LLPS, and RPA droplets were shown to colocalize with telomeres.[56] Similar to hSSB1 condensation, LLPS by RPA is enhanced by ssDNA. However, unlike that for hSSB1, ssRNA did not induce LLPS by RPA or become enriched inside condensates. Droplet formation by RPA is inhibited by phosphorylation, a regulatory mechanism also plausible for hSSB1 condensation, as hSSB1 is phosphorylated by multiple kinases.[5,54,57] The spatial regulation and potential co-existence of hSSB1 and RPA condensates is yet to be elucidated.

The role of hSSB1 and its discovered LLPS propensity in oxidative stress response is particularly relevant in the context of cancer cells that generally experience chronic oxidative stress. It is plausible that hSSB1's capability to form condensates in a redox-dependent manner supports cancer cell survival. Indeed, hSSB1 is upregulated in a large variety of cancers (Figure S20). In addition, hSSB1 was recently shown to be involved in DNA damage response and transcription regulation processes in prostate cancer.[58] Along these lines, small-molecule inhibitors of hSSB1's interaction with INTS3 and ssDNA have been identified and shown to inhibit the nuclear co-accumulation of INTS3 and hSSB1 upon genome damage[59] and to display selective cytotoxicity in U2OS osteosarcoma cells,[60] respectively. Considering that numerous anticancer agents act at least in part by generation of oxidative stress, targeting of hSSB1's LLPS propensity appears as a promising tool to sensitize cancer cells to oxidative stress without compromising the LLPS-independent functions of the protein.

Limitations of the study

We have shown that hSSB1 condensates colocalize with stress granules, and hSSB1 may play a regulatory role in stress granule formation. Further research is needed to uncover the precise function of hSSB1 in stress granules.

Redox-dependent nuclear hSSB1 condensation can also be presumed based on our results. Nuclear hSSB1 condensation could not be resolved in the current study due to high nuclear hSSB1 background signal in our immunocytochemical experiments.

We have also shown that all three cysteines of hSSB1 are needed for redox-dependent LLPS propensity, suggesting delicate allosteric regulation involving cysteine oxidation. We propose a model in which redox-dependent LLPS is brought about by cysteine oxidation–dependent IDR flexibility. More detailed structural studies are needed to corroborate this hypothesis.

RESOURCE AVAILABILITY

Lead contact

Further information and requests for resources and reagents should be directed to and will be fulfilled by the lead contact, M.K. (mihaly.kovacs@ttk.elte.hu).

Materials availability

This study did not generate new unique reagents. Plasmids generated in this study are available upon request. Any additional analysis information for this work is available by request to the lead contact. HFF-1 cell line was a gift by Ágota Apáti (HUN-REN Hungarian Research Network, Institute of Molecular Life Sciences).

Data and code availability

- All data reported in this article will be shared by the lead contact upon request. PDB files 4MZ9, 5D8E, 5D8F, 4OWW were obtained from the Protein DataBank. hSSB1 expression levels were obtained from Expression Atlas (https://www.ebi.ac.uk/gxa/home). Accession numbers are listed in the key resources table.

- This paper does not report original code.
- Any additional information required to reanalyze the data reported in this paper is available from the lead contact upon request.

ACKNOWLEDGMENTS

Funding: This work was supported by the "Momentum" Program of the Hungarian Academy of Sciences (LP2011-006/2011), ELTE KMOP-4.2.1/B-10-2011-0002, NKFIH K-123989, and NKFIH K-134595 grants to M.K. The project was supported by the NRDIO (VEKOP-2.3.3-15-2016-00007 to ELTE) grant. G.M.H. was supported by the Premium Postdoctoral Program of the Hungarian Academy of Sciences (PREMIUM-2017-17 to G.M.H.). Z.J.K. and J.P. were supported by the New National Excellence Program of the Ministry for Innovation and Technology (Grants ÚNKP-21-3 to Z.J.K. and ÚNKP-19-2 to J.P.), and the Co-operative Doctoral Program of the Ministry of Innovation and Technology financed from the National Research, Development and Innovation Fund. J.P. was supported by the Joseph Cours Scholarship of Eötvös Loránd University. This work was completed in the ELTE "SzintPlusz" Thematic Excellence Program supported by the Hungarian Ministry for Innovation and Technology, and also in the framework of Project no. 2018-1.2.1-NKP-2018-00005 implemented with the support provided from the National Research, Development and Innovation Fund of Hungary, financed under the 2018-1.2.1-NKP funding scheme.

AUTHOR CONTRIBUTIONS

G.M.H., J.P., Z.J.K., B.J., G.S., and M.K. conceptualized the project and designed experiments. J.P., Z.J.K., B.J., G.M.H., K.T., H.H.P., J.H., L.M., N.K., and S.T. performed experiments and analyzed the data. J.P., G.M.H., Z.J.K., and K.M. wrote the paper. All authors participated in revising the manuscript.

DECLARATION OF INTERESTS

The authors declare no competing interests.

STAR★METHODS

Detailed methods are provided in the online version of this paper and include the following:

- KEY RESOURCES TABLE
- EXPERIMENTAL MODEL AND STUDY PARTICIPANT DETAILS
  - Bacterial strains
  - Cell treatments, transfection, hSSB1 silencing
- METHOD DETAILS
  - General reaction conditions
  - Cloning, protein expression and purification
  - Fluorescent labeling of proteins
  - Fluorescence anisotropy titrations
  - Turbidity measurements
  - Epifluorescence microscopy for *in vitro* LLPS
  - Image processing for epifluorescence microscopy
  - *In vitro* oxidation experiments
  - Cell survival assay
  - Immunocytochemistry
  - Western blot
  - Epifluorescence and confocal microscopy of immunostained cells
  - Colocalization analysis
  - Determination of nuclear hSSB1 intensities and the number of SGs per cell
  - Cell typization
- QUANTIFICATION AND STATISTICAL ANALYSIS

SUPPLEMENTAL INFORMATION

Supplemental information can be found online at https://doi.org/10.1016/j.isci.2024.110788.

Received: May 22, 2024
Revised: June 6, 2024
Accepted: August 19, 2024
Published: August 22, 2024

REFERENCES

1. Shereda, R.D., Kozlov, A.G., Lohman, T.M., Cox, M.M., and Keck, J.L. (2008). SSB as an organizer/mobilizer of genome maintenance complexes. Crit. Rev. Biochem. Mol. Biol. *43*, 289–318. https://doi.org/10.1080/10409230802341296.
2. Antony, E., and Lohman, T.M. (2019). Dynamics of E. coli single stranded DNA binding (SSB) protein-DNA complexes. Semin. Cell Dev. Biol. *86*, 102–111. https://doi.org/10.1016/j.semcdb.2018.03.017.
3. Ashton, N.W., Loo, D., Paquet, N., O'Byrne, K.J., and Richard, D.J. (2016). Novel insight into the composition of human single-stranded DNA-binding protein 1 (hSSB1)-containing protein complexes. BMC Mol. Biol. *17*, 24. https://doi.org/10.1186/s12867-016-0077-5.
4. Bianco, P.R., Pottinger, S., Tan, H.Y., Nguyenduc, T., Rex, K., and Varshney, U. (2017). The IDL of E. coli SSB links ssDNA and protein binding by mediating protein-protein interactions. Protein Sci. *26*, 227–241. https://doi.org/10.1002/pro.3072.
5. Richard, D.J., Bolderson, E., Cubeddu, L., Wadsworth, R.I.M., Savage, K., Sharma, G.G., Nicolette, M.L., Tsvetanov, S., McIlwraith, M.J., Pandita, R.K., et al. (2008). Single-stranded DNA-binding protein hSSB1 is critical for genomic stability. Nature *453*, 677–681. https://doi.org/10.1038/nature06883.
6. Vidhyasagar, V., He, Y., Guo, M., Ding, H., Talwar, T., Nguyen, V., Nwosu, J., Katselis, G., and Wu, Y. (2016). C-termini are essential and distinct for nucleic acid binding of human NABP1 and NABP2. Biochim. Biophys. Acta *1860*, 371–383. https://doi.org/10.1016/j.bbagen.2015.11.003.

7. Lawson, T., El-Kamand, S., Kariawasam, R., Richard, D.J., Cubeddu, L., and Gamsjaeger, R. (2019). A Structural Perspective on the Regulation of Human Single-Stranded DNA Binding Protein 1 (hSSB1, OBFC2B) Function in DNA Repair. Comput. Struct. Biotechnol. J. *17*, 441–446. https://doi.org/10.1016/j.csbj.2019.03.014.
8. Paquet, N., Adams, M.N., Leong, V., Ashton, N.W., Touma, C., Gamsjaeger, R., Cubeddu, L., Beard, S., Burgess, J.T., Bolderson, E., et al. (2015). hSSB1 (NABP2/OBFC2B) is required for the repair of 8-oxo-guanine by the hOGG1-mediated base excision repair pathway. Nucleic Acids Res. *43*, 8817–8829. https://doi.org/10.1093/nar/gkv790.
9. Pandita, R.K., Chow, T.T., Udayakumar, D., Bain, A.L., Cubeddu, L., Hunt, C.R., Shi, W., Horikoshi, N., Zhao, Y., Wright, W.E., et al. (2015). Single-Strand DNA-Binding Protein SSB1 Facilitates TERT Recruitment to Telomeres and Maintains Telomere G-Overhangs. Cancer Res. *75*, 858–869. https://doi.org/10.1158/0008-5472.CAN-14-2289.
10. Skaar, J.R., Ferris, A.L., Wu, X., Saraf, A., Khanna, K.K., Florens, L., Washburn, M.P., Hughes, S.H., and Pagano, M. (2015). The Integrator complex controls the termination of transcription at diverse classes of gene targets. Cell Res. *25*, 288–305. https://doi.org/10.1038/cr.2015.19.
11. Feldhahn, N., Ferretti, E., Robbiani, D.F., Callen, E., Deroubaix, S., Selleri, L., Nussenzweig, A., and Nussenzweig, M.C. (2012). The hSSB1 orthologue Obfc2b is essential for skeletogenesis but dispensable for the DNA damage response *in vivo*. EMBO J. *31*, 4045–4056. https://doi.org/10.1038/emboj.2012.247.
12. Croft, L.V., Bolderson, E., Adams, M.N., El-Kamand, S., Kariawasam, R., Cubeddu, L., Gamsjaeger, R., and Richard, D.J. (2019). Human single-stranded DNA binding protein 1 (hSSB1, OBFC2B), a critical component of the DNA damage response. Semin. Cell Dev. Biol. *86*, 121–128. https://doi.org/10.1016/j.semcdb.2018.03.014.
13. Richard, D.J., Cubeddu, L., Urquhart, A.J., Bain, A., Bolderson, E., Menon, D., White, M.F., and Khanna, K.K. (2011). hSSB1 interacts directly with the MRN complex stimulating its recruitment to DNA double-strand breaks and its endo-nuclease activity. Nucleic Acids Res. *39*, 3643–3651. https://doi.org/10.1093/nar/gkq1340.
14. Yang, S.-H., Zhou, R., Campbell, J., Chen, J., Ha, T., and Paull, T.T. (2013). The SOSS1 single-stranded DNA binding complex promotes DNA end resection in concert with Exo1. EMBO J. *32*, 126–139. https://doi.org/10.1038/emboj.2012.314.
15. Croft, L.V., Ashton, N.W., Paquet, N., Bolderson, E., O'Byrne, K.J., and Richard, D.J. (2017). hSSB1 associates with and promotes stability of the BLM helicase. BMC Mol. Biol. *18*, 13. https://doi.org/10.1186/s12867-017-0090-3.
16. Bolderson, E., Petermann, E., Croft, L., Suraweera, A., Pandita, R.K., Pandita, T.K., Helleday, T., Khanna, K.K., and Richard, D.J. (2014). Human single-stranded DNA binding protein 1 (hSSB1/NABP2) is required for the stability and repair of stalled replication forks. Nucleic Acids Res. *42*, 6326–6336. https://doi.org/10.1093/nar/gku276.
17. Paquet, N., Adams, M.N., Ashton, N.W., Touma, C., Gamsjaeger, R., Cubeddu, L., Leong, V., Beard, S., Bolderson, E., Botting, C.H., et al. (2016). hSSB1 (NABP2/OBFC2B) is regulated by oxidative stress. Sci. Rep. *6*, 27446. https://doi.org/10.1038/srep27446.
18. Touma, C., Adams, M.N., Ashton, N.W., Mizzi, M., El-Kamand, S., Richard, D.J., Cubeddu, L., and Gamsjaeger, R. (2017). A data-driven structural model of hSSB1 (NABP2/OBFC2B) self-oligomerization. Nucleic Acids Res. *45*, 8609–8620. https://doi.org/10.1093/nar/gkx526.
19. Ren, W., Chen, H., Sun, Q., Tang, X., Lim, S.C., Huang, J., and Song, H. (2014). Structural basis of SOSS1 complex assembly and recognition of ssDNA. Cell Rep. *6*, 982–991. https://doi.org/10.1016/j.celrep.2014.02.020.
20. Huang, J., Gong, Z., Ghosal, G., and Chen, J. (2009). SOSS complexes participate in the maintenance of genomic stability. Mol. Cell *35*, 384–393. https://doi.org/10.1016/j.molcel.2009.06.011.
21. Skaar, J.R., Richard, D.J., Saraf, A., Toschi, A., Bolderson, E., Florens, L., Washburn, M.P., Khanna, K.K., and Pagano, M. (2009). INTS3 controls the hSSB1-mediated DNA damage response. J. Cell Biol. *187*, 25–32. https://doi.org/10.1083/jcb.200907026.
22. Li, Y., Bolderson, E., Kumar, R., Muniandy, P.A., Xue, Y., Richard, D.J., Seidman, M., Pandita, T.K., Khanna, K.K., and Wang, W. (2009). HSSB1 and hSSB2 form similar multiprotein complexes that participate in DNA damage response. J. Biol. Chem. *284*, 23525–23531. https://doi.org/10.1074/jbc.C109.039586.
23. El-Kamand, S., Adams, M.N., Matthews, J.M., Du Plessis, M., Crossett, B., Connolly, A., Breen, N., Dudley, A., Richard, D.J., Gamsjaeger, R., et al. (2023). The molecular details of a novel phosphorylation-dependent interaction between MRN and the SOSS complex. Protein Sci. *32*, e4782. https://doi.org/10.1002/pro.4782.
24. Harami, G.M., Kovács, Z.J., Pancsa, R., Pálinkás, J., Baráth, V., Tárnok, K., Málnási-Csizmadia, A., and Kovács, M. (2020). Phase separation by ssDNA binding protein controlled via protein−protein and protein−DNA interactions. Proc. Natl. Acad. Sci. USA *117*, 26206–26217. https://doi.org/10.1073/pnas.2000761117.
25. Zhao, T., Liu, Y., Wang, Z., He, R., Xiang Zhang, J., Xu, F., Lei, M., Deci, M.B., Nguyen, J., and Bianco, P.R. (2019). Super-resolution imaging reveals changes in Escherichia coli SSB localization in response to DNA damage. Gene Cell. *24*, 814–826. https://doi.org/10.1111/gtc.12729.
26. Sies, H., and Jones, D.P. (2020). Reactive oxygen species (ROS) as pleiotropic physiological signalling agents. Nat. Rev. Mol. Cell Biol. *21*, 363–383. https://doi.org/10.1038/s41580-020-0230-3.
27. Tuszynski, J.A., Wenger, C., Friesen, D.E., and Preto, J. (2016). An Overview of Sub-Cellular Mechanisms Involved in the Action of TTFields. Int. J. Environ. Res. Public Health *13*, 1128. https://doi.org/10.3390/ijerph13111128.
28. Kozlov, A.G., Cheng, X., Zhang, H., Shinn, M.K., Weiland, E., Nguyen, B., Shkel, I.A., Zytkiewicz, E., Finkelstein, I.J., Record, M.T., and Lohman, T.M. (2022). How Glutamate Promotes Liquid-liquid Phase Separation and DNA Binding Cooperativity of E. coli SSB Protein. J. Mol. Biol. *434*, 167562. https://doi.org/10.1016/j.jmb.2022.167562.
29. Dignon, G.L., Best, R.B., and Mittal, J. (2020). Biomolecular Phase Separation: From Molecular Driving Forces to Macroscopic Properties. Annu. Rev. Phys. Chem. *71*, 53–75. https://doi.org/10.1146/annurev-physchem-071819-113553.
30. Banani, S.F., Lee, H.O., Hyman, A.A., and Rosen, M.K. (2017). Biomolecular condensates: organizers of cellular biochemistry. Nat. Rev. Mol. Cell Biol. *18*, 285–298. https://doi.org/10.1038/nrm.2017.7.
31. Buchan, J.R., and Parker, R. (2009). Eukaryotic stress granules: the ins and outs of translation. Mol. Cell *36*, 932–941. https://doi.org/10.1016/j.molcel.2009.11.020.
32. Protter, D.S.W., and Parker, R. (2016). Principles and Properties of Stress Granules. Trends Cell Biol. *26*, 668–679. https://doi.org/10.1016/j.tcb.2016.05.004.
33. Yang, P., Mathieu, C., Kolaitis, R.-M., Zhang, P., Messing, J., Yurtsever, U., Yang, Z., Wu, J., Li, Y., Pan, Q., et al. (2020). G3BP1 Is a Tunable Switch that Triggers Phase Separation to Assemble Stress Granules. Cell *181*, 325–345.e28. https://doi.org/10.1016/j.cell.2020.03.046.
34. Ganini, D., Leinisch, F., Kumar, A., Jiang, J., Tokar, E.J., Malone, C.C., Petrovich, R.M., and Mason, R.P. (2017). Fluorescent proteins such as eGFP lead to catalytic oxidative stress in cells. Redox Biol. *12*, 462–468. https://doi.org/10.1016/j.redox.2017.03.002.
35. Youn, J.-Y., Dyakov, B.J.A., Zhang, J., Knight, J.D.R., Vernon, R.M., Forman-Kay, J.D., and Gingras, A.-C. (2019). Properties of Stress Granule and P-Body Proteomes. Mol. Cell *76*, 286–294. https://doi.org/10.1016/j.molcel.2019.09.014.
36. Luo, Y., Na, Z., and Slavoff, S.A. (2018). P-Bodies: Composition, Properties, and Functions. Biochemistry *57*, 2424–2431. https://doi.org/10.1021/acs.biochem.7b01162.
37. Johnson, M.E., Grassetti, A.V., Taroni, J.N., Lyons, S.M., Schweppe, D., Gordon, J.K., Spiera, R.F., Lafyatis, R., Anderson, P.J., Gerber, S.A., and Whitfield, M.L. (2016). Stress granules and RNA processing bodies are novel autoantibody targets in systemic sclerosis. Arthritis Res. Ther. *18*, 27. https://doi.org/10.1186/s13075-016-0914-4.
38. Loor, G., Kondapalli, J., Schriewer, J.M., Chandel, N.S., Vanden Hoek, T.L., and Schumacker, P.T. (2010). Menadione triggers cell death through ROS-dependent mechanisms involving PARP activation without requiring apoptosis. Free Radic. Biol. Med. *49*, 1925–1936. https://doi.org/10.1016/j.freeradbiomed.2010.09.021.
39. Wufuer, R., Fan, Z., Yuan, J., Zheng, Z., Hu, S., Sun, G., and Zhang, Y. (2022). Distinct Roles of Nrf1 and Nrf2 in Monitoring the Reductive Stress Response to Dithiothreitol (DTT). Antioxidants *11*, 1535. https://doi.org/10.3390/antiox11081535.
40. Montecucco, A., Zanetta, F., and Biamonti, G. (2015). Molecular mechanisms of etoposide. EXCLI J *14*, 95–108. https://doi.org/10.17179/excli2015-561.
41. Schieber, M., and Chandel, N.S. (2014). ROS function in redox signaling and oxidative stress. Curr. Biol. *24*, R453–R462. https://doi.org/10.1016/j.cub.2014.03.034.
42. Maynard, S., Schurman, S.H., Harboe, C., de Souza-Pinto, N.C., and Bohr, V.A. (2009). Base excision repair of oxidative DNA damage and association with cancer and aging. Carcinogenesis *30*, 2–10. https://doi.org/10.1093/carcin/bgn250.
43. Paulsen, C.E., and Carroll, K.S. (2010). Orchestrating redox signaling networks through regulatory cysteine switches. ACS

Chem. Biol. *5*, 47–62. https://doi.org/10.1021/cb900258z.

44. Poole, L.B. (2015). The basics of thiols and cysteines in redox biology and chemistry. Free Radic. Biol. Med. *80*, 148–157. https://doi.org/10.1016/j.freeradbiomed.2014.11.013.
45. El-Kamand, S., Jergic, S., Lawson, T., Kariawasam, R., Richard, D.J., Cubeddu, L., and Gamsjaeger, R. (2020). A biophysical and structural analysis of DNA binding by oligomeric hSSB1 (NABP2/OBFC2B). Preprint at bioRxiv. https://doi.org/10.1101/2020.08.26.269084.
46. Klomsiri, C., Karplus, P.A., and Poole, L.B. (2011). Cysteine-based redox switches in enzymes. Antioxid. Redox Signal. *14*, 1065–1077. https://doi.org/10.1089/ars.2010.3376.
47. Huang, X., Chen, S., Li, W., Tang, L., Zhang, Y., Yang, N., Zou, Y., Zhai, X., Xiao, N., Liu, W., et al. (2021). ROS regulated reversible protein phase separation synchronizes plant flowering. Nat. Chem. Biol. *17*, 549–557. https://doi.org/10.1038/s41589-021-00739-0.
48. Kato, M., Yang, Y.-S., Sutter, B.M., Wang, Y., McKnight, S.L., and Tu, B.P. (2019). Redox State Controls Phase Separation of the Yeast Ataxin-2 Protein via Reversible Oxidation of Its Methionine-Rich Low-Complexity Domain. Cell *177*, 711–721.e8. https://doi.org/10.1016/j.cell.2019.02.044.
49. Kovács, Z.J., Harami, G.M., Pálinkás, J., Kuljanishvili, N., Hegedüs, J., Harami-Papp, H., Mahmudova, L., Khamisi, L., Szakács, G., and Kovács, M. (2024). DNA-dependent phase separation by human SSB2 (NABP1/OBFC2A) protein points to adaptations to eukaryotic genome repair processes. Protein Sci. *33*, e4959. https://doi.org/10.1002/pro.4959.
50. Marmor-Kollet, H., Siany, A., Kedersha, N., Knafo, N., Rivkin, N., Danino, Y.M., Moens, T.G., Olender, T., Sheban, D., Cohen, N., et al. (2020). Spatiotemporal Proteomic Analysis of Stress Granule Disassembly Using APEX Reveals Regulation by SUMOylation and Links to ALS Pathogenesis. Mol. Cell *80*, 876–891.e6. https://doi.org/10.1016/j.molcel.2020.10.032.
51. Danino, Y.M., Molitor, L., Rosenbaum-Cohen, T., Kaiser, S., Cohen, Y., Porat, Z., Marmor-Kollet, H., Katina, C., Savidor, A., Rotkopf, R., et al. (2023). BLM helicase protein negatively regulates stress granule formation through unwinding RNA G-quadruplex structures. Nucleic Acids Res. *51*, 9369–9384. https://doi.org/10.1093/nar/gkad613.
52. Bravard, A., Campalans, A., Vacher, M., Gouget, B., Levalois, C., Chevillard, S., and Radicella, J.P. (2010). Inactivation by oxidation and recruitment into stress granules of hOGG1 but not APE1 in human cells exposed to sub-lethal concentrations of cadmium. Mutat. Res. *685*, 61–69. https://doi.org/10.1016/j.mrfmmm.2009.09.013.
53. Vidhyasagar, V., He, Y., Guo, M., Talwar, T., Singh, R.S., Yadav, M., Katselis, G., Vizeacoumar, F.J., Lukong, K.E., and Wu, Y. (2018). Biochemical characterization of INTS3 and C9ORF80, two subunits of hNABP1/2 heterotrimeric complex in nucleic acid binding. Biochem. J. *475*, 45–60. https://doi.org/10.1042/BCJ20170351.
54. Long, Q., Sebesta, M., Sedova, K., Haluza, V., Alagia, A., Liu, Z., Stefl, R., and Gullerova, M. (2023). The phosphorylated trimeric SOSS1 complex and RNA polymerase II trigger liquid-liquid phase separation at double-strand breaks. Cell Rep. *42*, 113489. https://doi.org/10.1016/j.celrep.2023.113489.
55. Xu, C., Li, C., Chen, J., Xiong, Y., Qiao, Z., Fan, P., Li, C., Ma, S., Liu, J., Song, A., et al. (2023). R-loop-dependent promoter-proximal termination ensures genome stability. Nature *621*, 610–619. https://doi.org/10.1038/s41586-023-06515-5.
56. Spegg, V., Panagopoulos, A., Stout, M., Krishnan, A., Reginato, G., Imhof, R., Roschitzki, B., Cejka, P., and Altmeyer, M. (2023). Phase separation properties of RPA combine high-affinity ssDNA binding with dynamic condensate functions at telomeres. Nat. Struct. Mol. Biol. *30*, 451–462. https://doi.org/10.1038/s41594-023-00932-w.
57. Ashton, N.W., Paquet, N., Shirran, S.L., Bolderson, E., Kariawasam, R., Touma, C., Fallahbaghery, A., Gamsjaeger, R., Cubeddu, L., Botting, C., et al. (2017). hSSB1 phosphorylation is dynamically regulated by DNA-PK and PPP-family protein phosphatases. DNA Repair *54*, 30–39. https://doi.org/10.1016/j.dnarep.2017.03.006.
58. Adams, M.N., Croft, L.V., Urquhart, A., Saleem, M.A.M., Rockstroh, A., Duijf, P.H.G., Thomas, P.B., Ferguson, G.P., Najib, I.M., Shah, E.T., et al. (2023). hSSB1 (NABP2/OBFC2B) modulates the DNA damage and androgen-induced transcriptional response in prostate cancer. Prostate *83*, 628–640. https://doi.org/10.1002/pros.24496.
59. Barbhuiya, T.K., Beard, S., Shah, E.T., Mason, S., Bolderson, E., O'Byrne, K., Guddat, L.W., Richard, D.J., Adams, M.N., and Gandhi, N.S. (2024). Targeting the hSSB1-INTS3 Interface: A Computational Screening Driven Approach to Identify Potential Modulators. ACS Omega *9*, 8362–8373. https://doi.org/10.1021/acsomega.3c09267.
60. Schuurs, Z.P., Martyn, A.P., Soltau, C.P., Beard, S., Shah, E.T., Adams, M.N., Croft, L.V., O'Byrne, K.J., Richard, D.J., and Gandhi, N.S. (2023). An Exploration of Small Molecules That Bind Human Single-Stranded DNA Binding Protein 1. Biology *12*, 1405. https://doi.org/10.3390/biology12111405.
61. Harami, G.M., Pálinkás, J., Seol, Y., Kovács, Z.J., Gyimesi, M., Harami-Papp, H., Neuman, K.C., and Kovács, M. (2022). The toposiomerase IIIalpha-RMI1-RMI2 complex orients human Bloom's syndrome helicase for efficient disruption of D-loops. Nat. Commun. *13*, 654. https://doi.org/10.1038/s41467-022-28208-9.
62. Bolte, S., and Cordelières, F.P. (2006). A guided tour into subcellular colocalization analysis in light microscopy. J. Microsc. *224*, 213–232. https://doi.org/10.1111/j.1365-2818.2006.01706.x.
63. Stringer, C., Wang, T., Michaelos, M., and Pachitariu, M. (2021). Cellpose: a generalist algorithm for cellular segmentation. Nat. Methods *18*, 100–106. https://doi.org/10.1038/s41592-020-01018-x.

STAR★METHODS

KEY RESOURCES TABLE

REAGENT or RESOURCE	SOURCE	IDENTIFIER
Antibodies		
Anti-NABP2 antibody produced in rabbit	Sigma-Aldrich	Cat#HPA044615; RRID: AB_10795884
Anti-G3BP antibody	Abcam	Cat#ab56574; RRID: AB_941699
Anti-Sk1-Hedls (p70 S6 kinase/S6K1 Antibody)	Santa Cruz Biotechnology	Cat#sc-8418; RRID: AB_628094
Anti-GAPDH antibody produced in rabbit	Sigma-Aldrich	Cat#G9545; RRID: AB_796208
Goat anti-Mouse IgG (H+L) Highly Cross-Adsorbed Secondary Antibody, Alexa Fluor™ 633	Thermo Fisher	Cat#A-21052; RRID: AB_2535719
Goat anti-Rabbit IgG (H+L) Cross-Adsorbed Secondary Antibody, Alexa Fluor™ 488	Thermo Fisher	Cat#A-11008; RRID: AB_143165
Peroxidase AffiniPure™ Goat Anti-Rabbit IgG (H+L)	Jackson Immunoresearch	Cat#111-035-003; RRID: AB_2313567
Peroxidase AffiniPure™ Goat Anti-Mouse IgG (H+L)	Jackson Immunoresearch	Cat#115-035-003; RRID: AB_10015289
Bacterial and virus strains		
Mix & Go! Competent Cells - DH5 Alpha	Zymo Research	Cat#T3007
Rosetta™ 2(DE3) Competent Cells	Merck	Cat#71397
Chemicals, peptides, and recombinant proteins		
RPMI-1640 Medium	Sigma-Aldrich	Cat#R8758
DMEM, high glucose	Thermo Fisher	Cat#41965062
5-(Iodoacetamido)fluorescein	Sigma-Aldrich	Cat#I9271
Alexa Fluor™ 488 NHS Ester (Succinimidyl Ester)	Thermo Fisher	Cat#A20000
Alexa Fluor™ 647 NHS Ester (Succinimidyl Ester)	Thermo Fisher	Cat#A20006
Blocking Reagent	Roche	Cat#11096176001
Mowiol® 4-88	Polysciences	Cat#25213-24-5
Hoechst 33342	Thermo Fisher	Cat#62249
DAPI	Sigma-Aldrich	Cat#D9542
H_2O_2	VWR	Cat#VWRC23619.297
DTT	Thermo Fisher	Cat#R0862
Menadione sodium bisulfite	Sigma-Aldrich	Cat#M2518
Etoposide	Sigma-Aldrich	Cat#E1383
Potassium bromate	Sigma-Aldrich	Cat#309087
Sodium arsenite solution	Sigma-Aldrich	Cat#1.06277
Diamide	Sigma-Aldrich	Cat#D3648
hSSB1	Purified by us	N/A
hSSB1 C41S	Purified by us	N/A
hSSB1 C81S	Purified by us	N/A
hSSB1 C99S	Purified by us	N/A
hSSB1 C41S-C81S	Purified by us	N/A
hSSB1 C41S-C99S	Purified by us	N/A
hSSB1 C81S-C99S	Purified by us	N/A
hSSB1-C41S-C81S-C99S	Purified by us	N/A
hSSB1-dIDR	Purified by us	N/A
hSSB2	Purified by us	N/A
INTS3	Purified by us	N/A

(*Continued on next page*)

Continued

REAGENT or RESOURCE	SOURCE	IDENTIFIER
INIP	Purified by us	N/A
BLM	Purified by us	N/A
EGFP	Purified by us	N/A
hOGG1	Abcam	Cat#ab98249
G3BP1	Abcam	Cat#ab103304
Critical commercial assays		
QuikChange II XL Site-Directed Mutagenesis Kit	Agilent	Cat#200522
HisPur™ Ni-NTA Resin	Thermo Fisher	Cat#88222
HiTrap Heparin HP affinity columns	Cytiva	Cat#17040601
GST·Bind™ Resin	Milllipore	Cat#70541
Amicon® Ultra Centrifugal Filter, 10 kDa MWCO	Milllipore	Cat#UFC9010
Amicon® Ultra Centrifugal Filter, 30 kDa MWCO	Millipore	Cat#UFC5030
Amicon® Ultra Centrifugal Filter, 100 kDa MWCO	Milllipore	Cat#UFC9100
4x Laemmli Sample Buffer	Bio-Rad	Cat#1610747
Mini-Protean TGX gels 4-20%	Bio-Rad	Cat#4561094
Pierce™ Bradford Plus Protein Assay Reagent	Thermo Fisher	Cat#23200
PageBlue™ Protein Staining Solution	Thermo Fisher	Cat#24620
Disposable PD 10 Desalting Columns	Sigma-Aldrich	Cat#GE17-0851-01
MICROPLATE, 384 WELL, PS, F-BOTTOM	Greiner	Cat#784900
µ-Slide 15 Well 3D	Ibidi	Cat#81506
25 nM ON-TARGETplus human NABP2 siRNA SMARTpool	Horizon	Cat#L-014288-01-0005
ON-TARGETplus Non-targeting Control Pool	Horizon	Cat#D-001810-10-05
PrestoBlue™ Cell Viability Reagent	Thermo Fisher	Cat#A13261
Immobilon Crescendo Western HRP substrate, 100 mL	Sigma-Aldrich	Cat#WBLUR0500
Experimental models: Cell lines		
HeLa	ATCC	Cat#CCL-2; RRID: CVCL_0030
HEK293T	ATCC	Cat#CRL-3216; RRID: CVCL_0063
HFF-1	gift by Ágota Apáti (Hungarian Research Network, Institute of Molecular Life Science)	N/A
Oligonucleotides		
PCR primers for generating hSSB1 variants	Table S2	N/A
Deoxythymidine oligonucleotides (dT18-dT96)	Sigma-Aldrich	custom DNA oligo
Cy3-dT45	Sigma-Aldrich	custom DNA oligo
Cy3-dT79	Sigma-Aldrich	custom DNA oligo
Uridine RNA oligonucleotides (U32, U41)	Sigma-Aldrich	custom RNA oligo
Cy3-labeled nonhomopolymeric 41-mer ssRNA	Sigma-Aldrich	custom RNA oligo
3′-fluorescein-labeled 36-mer ssDNA (used for fluorescence anisotropy titrations)	Sigma-Aldrich	custom DNA oligo
3′-fluorescein-labeled 36-mer ssRNA (used for fluorescence anisotropy titrations)	Sigma-Aldrich	custom RNA oligo
Recombinant DNA		
pET29a-hNABP2 (hSSB1)	gifts from Yuliang Wu (College of Medicine, University of Saskatchewan)	Addgene #128307; RRID: Addgene_128307; ref.6

(*Continued on next page*)

Continued

REAGENT or RESOURCE	SOURCE	IDENTIFIER
pET29a-hNABP1 (hSSB2)	gifts from Yuliang Wu (College of Medicine, University of Saskatchewan)	Addgene #128306; RRID: Addgene_128306; ref.6
pET28a-C9ORF80	gifts from Yuliang Wu (College of Medicine, University of Saskatchewan)	Addgene #128418; RRID: Addgene_128418; ref.53
pGEX-6P-1-INTS3-FL	gifts from Yuliang Wu (College of Medicine, University of Saskatchewan)	Addgene #128415; RRID: Addgene_128415; ref. 53
pEGFP-C1	Clontech	Cat#6084-1
Software and algorithms		
ImageJ	https://imagej.net/software/fiji/downloads	RRID: SCR_002285
GelQuant Pro	DNR Bio Imaging Ltd.	v12
ZEN Microscopy Software	Zeiss	N/A
Cellpose	https://www.cellpose.org/	N/A
OriginPro	OriginLab Corporation	2018
Biorender	Biorender	RRID: SCR_018361
Other		
hSSB1 crystal structure	Protein Data Bank	4MZ9
hSSB1 crystal structure	Protein Data Bank	5D8E
hSSB1 crystal structure	Protein Data Bank	5D8F
hSSB1 crystal structure	Protein Data Bank	4OWW
hSSB1 expression levels	Expression Atlas	https://www.ebi.ac.uk/gxa/home ensg00000139579 (NABP2)

EXPERIMENTAL MODEL AND STUDY PARTICIPANT DETAILS

Bacterial strains

E. coli DH5α cells were used for cloning. Rosetta 2(DE3) strain was used for protein expression. Cells were grown in Lysogeny Broth at 37°C.

Cell treatments, transfection, hSSB1 silencing

HeLa, HEK293T (both female origin), and HFF-1 (male origin) cells were maintained at 37°C under 5% CO_2 atmosphere in RPMI-1640 medium (for HeLa) and DMEM (for HEK293T and HFF-1) supplemented with fetal bovine serum, gentamicin and amphotericin B.

For plasmid transfection, 25,000 cells were seeded onto plasma-sterilized, polylysine-treated coverslips in wells of a 24-well plate. Cells were transfected on the next day with pEGFP-C1 or pEGFP-C1-hSSB1 plasmids, encoding EGFP or EGFP-fused hSSB1 under the regulation of a CMV promoter. 1 μg of plasmid was transfected via lipofection using Lipofectamine 2000 reagent, in medium free of antibiotics and antifungals. Normal medium was replaced after 4 h. After 24 h of expression, cells were treated in serum free media as indicated.

For non-transfected cells, 25,000 cells were seeded into wells of a confocal chamber slide and treated the next day in serum free media as indicated. For hSSB1 silencing, 25,000 cells were seeded onto plasma-sterilized, polylysine-treated coverslips in wells of a 24-well plate. Cells were transfected on the next day with 25 nM ON-TARGETplus human NABP2 siRNA SMARTpool using DharmaFect transfection reagent, in a medium free of antibiotics and antifungals. For non-targeting RNA control, the ON-TARGETplus Non-targeting Control Pool was used. Normal medium was replaced after 6 h. 48 h after transfection, cells were lyzed for Western blot analysis or treated in serum free media as indicated.

For treatments, H_2O_2 was applied for 2 h in indicated concentrations (0.1, 0.3 or 1 mM). In Figure S16, H_2O_2 was applied for 0.5 h or 2 h at 1 mM concentration. For serum deprivation experiments (Figure S17), normal medium was changed to serum-free medium for indicated times. Other stress agents were used as follows: $KBrO_3$, 30 mM for 2 h; $NaAsO_2$, 0.5 mM for 2 h; menadione sodium bisulfite, 100 μM for 4 h; DTT, 1 mM for 2 h; etoposide, 100 μM for 2 h. All agents were applied in serum-free medium.

METHOD DETAILS

General reaction conditions

Unless otherwise stated, *in vitro* measurements were performed at 25°C in LLPS buffer containing 25 mM Tris-HCl pH 7.4, 10 mM $MgCl_2$, 50 mM KCl, supplemented with 0.003 % (980 μM) H_2O_2 for oxidizing conditions, or 1 mM DTT for reducing conditions. LLPS buffer omitting

$MgCl_2$ and KCl (denoted as "no salt LLPS buffer") was used where indicated. We note that the latter experiments contained 1.7 mM KCl and 3.4 mM $MgCl_2$ originating from the storage buffer of hSSB1.

Cloning, protein expression and purification

pET29a-hNABP2 (hSSB1), pET29a-hNABP1 (hSSB2), pET28a-C9ORF80, and pGEX-6P-1-INTS3-FL were gifts from Yuliang Wu (Addgene plasmids #128307, 128306, 128418, and 128415, respectively).[6,53] pET29a-hSSB1 contained a point mutation coding for an Y85C substitution, which was restored to WT tyrosine using QuikChange mutagenesis. QuikChange results were verified by DNA sequencing. Expression and purification of hSSB1 and hSSB2 fused to a C-terminal histidine-tag were performed as described in ref.[5,6] with modifications as follows. In the case of hSSB1, Ni-NTA beads were equilibrated with buffer A (25 mM Tris-HCl pH 8.0, 500 mM NaCl, 10 % glycerol, 0.1 % TWEEN 20). Loaded column was washed with 10 column volumes of buffer B (25 mM Tris-HCl pH 8.0, 50 mM NaCl, 10 % glycerol, 0.1 % TWEEN 20) supplemented with 50 mM imidazole. Protein was eluted with buffer B containing 250 mM imidazole and loaded on HiTrap Heparin column equilibrated with HP1 buffer (25 mM Tris-HCl pH 8.0, 50 mM NaCl, 10 % glycerol). Elution was achieved with HP2 buffer (25 mM Tris-HCl pH 8.0, 1 M NaCl, 10 % glycerol). Purified protein samples were concentrated using Amicon Ultra 10K spin column and dialyzed against Storage buffer (25 mM Tris-HCl pH 8.0, 50 mM KCl, 100 mM $MgCl_2$, 10 % glycerol, 1 mM DTT). Plasmids coding for hSSB1 variants were generated from the Y85C substitution-corrected pET29a-hSSB1 vector using the QuikChange mutagenesis kit, and hSSB1 variant proteins were purified as WT hSSB1. In case of hSSB1-IDR, a stop codon was introduced after the codon coding for aa 96. Mutagenesis was verified by DNA sequencing. Primers are listed in Table S2. In the case of hSSB2, only nickel affinity chromatography was applied.

INTS3 and INIP were purified as described[53] with modifications for INTS3 as follows. After sonication, GST-tagged INTS3 was loaded onto Glutathione Agarose column equilibrated with buffer A (25 mM Tris-HCl pH 8.0, 500 mM NaCl, 1 mM EDTA, 1 mM DTT, 0.2 % Tween 20, 10 % glycerol). Loaded column was washed with 2 column volumes of buffer B (25 mM Tris-HCl pH 8.0, 150 mM NaCl, 1 mM DTT, 0.2 % Tween 20, 10 % glycerol). Precision protease (10 unit/ml) was introduced in buffer B on column and INTS3 was digested overnight. Tag-free protein was eluted with buffer B, then concentrated with Amicon Ultra 100K spin column and dialyzed against Storage buffer (25 mM Tris-HCl pH 8.0, 50 mM NaCl, 10 % glycerol, 1 mM DTT).

Plasmids, expression, and purification of EcSSB, human BLM and EGFP constructs were described in.[24,61] Recombinant hOGG1 (ab98249) and G3BP1 (ab103304) were purchased from Abcam.

Purity of samples was checked by tris-glycine based gradient SDS-PAGE (Mini-Protean TGX 4-20 %, Bio-Rad) for all constructs. Bradford method was used for concentration measurement of proteins. Purified proteins were frozen in droplets and stored in liquid N_2.

pEGFP-C1 plasmid, used for transfection of HeLa cells, was obtained from Clontech. The hSSB1 coding sequence was amplified by PCR and cloned upstream of EGFP to fuse hSSB1 to the N-terminus of EGFP. Primers are listed in Table S2. Constructs were verified by DNA sequencing.

Fluorescent labeling of proteins

hSSB2 was labeled with 5-IAF (5-iodoacetamido-fluorescein) on the intrinsic cysteines. hSSB2 Storage buffer (25 mM Tris-HCl pH 8.0, 50 mM NaCl, 100 mM $MgCl_2$, 10% glycerol, 1 mM DTT) was exchanged to a storage buffer omitting DTT using a PD10 gel filtration column. IAF was applied at 1.5-fold molar excess compared to hSSB2. The labeling reaction was performed for 3.5 h in argon atmosphere, at room temperature. The labeled protein was purified with a PD10 column pre-equilibrated with hSSB2 storage buffer and dialyzed against storage buffer to remove residual free dye.

INIP, hOGG1, and G3BP1 were labeled on their N-termini with AF488 (Alexa Fluor 488 carboxylic acid succinimidyl ester). Storage buffer was exchanged to Labeling buffer (50 mM MES pH 6.5, 50 mM KCl, 10% glycerol) by dialysis. AF488 was introduced in 4-fold molar excess over protein. Labeling process was performed for 5 h at room temperature. Reaction was stopped by 50 mM Tris-HCl final concentration. For INIP, the labeled protein was purified using a PD10 column pre-equilibrated with INIP Storage buffer (25 mM Tris-HCl pH 8, 150 mM KCl, 10% glycerol). and was dialyzed against Storage buffer and repetitively filtered using an Amicon Ultra 10K spin column to remove residual free dye. Labeled hOGG1 and G3BP1 were repetitively filtered on Amicon Ultra 10K and 30K to exchange labeling buffer to storage buffers provided by manufacturers.

hSSB1 and INTS3 proteins were labeled with AF647 (Alexa Fluor 647 carboxylic acid succinimidyl ester). Proteins were dialyzed against Labeling buffer (50 mM MES pH 6.5, 50 mM KCl, 100 mM $MgCl_2$, 5 mM DTT). AF647 was applied at 1.5-fold molar excess over proteins. Labeling reactions were carried out for 3.5 h in the case of both proteins. Reactions were stopped by the addition of 50 mM Tris-HCl final concentration. The labeled proteins were purified with a PD10 column pre-equilibrated with Storage buffers (hSSB1: 25 mM Tris-HCl pH 8.0, 50 mM NaCl, 100 mM $MgCl_2$, 10% glycerol, 1 mM DTT; INTS3: 25 mM Tris-HCl pH 8.0, 50 mM NaCl, 10% glycerol, 1 mM DTT). Samples were dialyzed against Storage buffers and in the case of INTS3 an Amicon Ultra 100K spin column was applied to remove residual free dye.

Protein concentrations were determined by Bradford method. Labeling efficiency was determined by visible light spectrometry using $\varepsilon 494$ = 80000 for 5-IAF, $\varepsilon 488$ = 73000 M^{-1} cm^{-1} for AF488, and $\varepsilon 647$ = 270000 M^{-1} cm^{-1} for AF647. Labeling ratios were 60% for hSSB2, 17% for INIP, 10% for hSSB1, 51% for hOGG1, 55% for G3BP1, and 9.6% for INTS3.

Protein purity was checked for all constructs using SDS-PAGE. All constructs were frozen in liquid N2 in small aliquots and stored at -80°C. Labeling methods for BLM and EcSSB are described in.[24]

Fluorescence anisotropy titrations

DNA and RNA binding was measured in FP buffer (25 mM Tris-HCl pH 7.4, 50 mM KCl, 1 mM DTT) with 10 nM of 3'-fluorescein-labeled 36-mer ssDNA or 36-mer ssRNA oligonucleotide (ssDNA: ATTTTTGCGGATGGCTTAGAGCTTAATTGCGCAACG-fluorescein, ssRNA: AUUUUUGCGGAUGGCUUAGAGCUUAAUUGCGCAACG -fluorescein). Fluorescence anisotropy of 12-µl samples was measured in 384-well low-volume nontransparent microplates (Greiner) at 25°C in a Synergy H4 Hybrid Multi-Mode Microplate Reader (BioTek) and converted to anisotropy values. Fits were performed using the Hill equation (n = 3 independent measurements).

Turbidity measurements

Turbidity (light depletion at 600-nm wavelength) titrations were performed at indicated hSSB1 concentrations in the presence of indicated ssDNA ($dT_{18\text{-}96}$ homopolymer, single-stranded deoxythymidine oligonucleotides) or ssRNA (U_{32}, 32mer single-stranded uridine oligonucleotide) concentrations and were measured in a Tecan Infinite Nano+ plate reader instrument at 25°C. For measurements at low micromolar H_2O_2 concentrations (Figure 2E), DTT was removed from hSSB1 storage buffer using a 10K spin column and DTT concentration was remeasured with DTNB (Ellman's Reagent) to a final concentration of 0.4 µM.

Epifluorescence microscopy for *in vitro* LLPS

A Nikon Eclipse Ti-E TIRF microscope was used in epifluorescence mode with apo TIRF 100x oil immersion objective (numerical aperture (NA) = 1.49). A Cyan 488-nm laser (Coherent), a 543-nm laser (25-LGP-193–230, Melles Griot) and a 642-nm laser (56RCS/S2799, Melles Griot) were used for excitation. Fluorescence was deflected to a ZT405/488/561/640rpc BS dichroic mirror and recorded by a Zyla sCMOS (ANDOR) camera. Images were captured using the imaging software NIS-Elements AR (Advanced Research) 4.50.00. Experiments were recorded with 2x2 binning and 200-ms laser exposure optical setup. 20-µl volumes of samples were introduced into µ-Slides at 25°C. Sample components were mixed freshly and incubated for 1 h before imaging, unless indicated otherwise.

In the absence of nucleic acids (Figures 2A and S4E) and for measurements shown in Figures 4B and S6D, 5 µM hSSB1 and 0.1 µM Alexa Fluor 647-labeled hSSB1 ($hSSB1^{AF647}$) were mixed. All other nucleic acid-containing experiments were carried out using 5 µM hSSB1 (wild-type or variants) in the presence of 2 µM ssDNA (dT_{79}, containing 100 nM Cy3-labeled dT_{79} or dT_{45}, containing 100 nM Cy3-labeled dT_{45}) or 2 µM ssRNA (U41; 41-mer uridine homopolymer, containing 100 nM Cy3-labeled nonhomopolymeric 41-mer ssRNA) unless indicated otherwise. Figure S2 shows that labeled ssDNA can readily enter hSSB1 droplets, thus it can be used for LLPS visualization without the need for protein labeling. For droplet fusion experiment, chambers were treated with 1.5 mg/ml Blocking Reagent (Roche) for 30 min before introducing hSSB1. Fusions were monitored at 4-5 sec intervals.

For multiprotein co-condensation experiments (Figure 4), 180 nM labeled protein interaction partners were used either alone or together with 5 µM hSSB1 containing 0.1 µM AlexaFluor647-hSSB1. Each experiment contained also 2 µM dT_{79} (or 2 µM U_{41} in Figure S11B) and 980 µM H_2O_2. In the case of labeled hSSB2, BLM, hOGG1, G3BP1, EGFP, and fluorescein dye molecules, hSSB1 was incubated for 1 hour before introducing fluorescent partners, then co-incubated with partners for additional 30 min before imaging. Since INTS3 and hSSB1 were both labeled with AlexaFluor647, in experiments containing labeled INTS3, labeled ssDNA (2 µM dT_{79} containing 0.1 µM Cy3-dT_{79}) was used to visualize hSSB1 droplets (5 µM unlabeled protein). Furthermore, in experiments containing INTS3 and/or INIP partners, hSSB1 was co-incubated with partners for 2 hours before imaging. For the INIP + INTS3 complex-containing sample, 180 nM labeled INIP and 1 µM unlabeled INTS3 were used.

Image processing for epifluorescence microscopy

ImageJ software was used to analyze unprocessed images. Image stack was generated from raw images of a given experiment to set brightness and contrast equally, using the automatic detection algorithm. Images were background corrected with the built-in rolling ball background correction, unless otherwise indicated. Montage was generated from stack of a given experiment to visually represent the changing conditions of the experimental set.

Since hSSB1 condensates spread out on the surface of microscope slide over time, instead of droplet size analysis[24] we analyzed the mean grey values and total areas of droplets. Stack of 3 images was generated for each condition. Middle ROI (Region of Interest) (area: 600 x 600 pixels; X,Y coordinates from left, uppermost pixel position: 300 pixels) of every stack was selected for technical reasons. Mean grey values (sum of intensity values from all pixels divided by the number of pixels) were measured for each middle ROI using the Stack Fitter plugin, then averaged for each condition separately. For determination of the total droplet area of middle ROIs, background correction thresholds were set using the built-in image thresholder of ImageJ. The particle analyzer algorithm (smallest detected size was set to 0.2 μm^2, circularity 0.1–1) was applied to outline the distinct fluorescent spot areas of each middle ROI of a stack, which were added together separately and the distinct ROI values of one condition were averaged to get the total droplet area in μm^2.

In vitro oxidation experiments

20 µM of protein was incubated in LLPS buffer for 45 minutes at room temperature with indicated H_2O_2 concentrations. Covalent oligomers were separated via tris-glycine based SDS-PAGE on a 10% polyacrylamide gel. Electrophoresis was performed at 200 V constant voltage for 90 min. Gels were rinsed with ddH_2O and stained overnight with PageBlue Protein Staining Solution and de-stained in ddH_2O. Fraction of monomers and dimers were analyzed by pixel densitometry using the GelQuant Pro v12 software.

Cell survival assay

10,000 cells were seeded in wells of a 96-well plate in RPMI medium supplemented with 10% FBS. After two days cells were treated with H_2O_2 for 1 h. PrestoBlue reagent was added to a final concentration of 10% and was incubated for additional 1 h. PrestoBlue incubation time was taken into account for total treatment time. Fluorescence was measured at 590 nm with 560 nm excitation wavelength.

Immunocytochemistry

Immediately after treatment, cells were washed with DPBS (Dulbecco's Phosphate Buffered Saline) and fixed with 4 % PFA for 20 minutes. Membrane permeabilization was achieved with 0.5% Triton-X for 5 min. Samples were blocked with 2% BSA for 1 h at room temperature, and primary antibodies were applied overnight in blocking reagent at 4°C. Anti-hSSB1 (HPA044615), anti-G3BP1 (ab56574), and anti-SK1-Hedls (sc-8418) were purchased from Sigma-Aldrich, Abcam, and Santa Cruz Biotechnology, respectively. Secondary antibodies (anti-mouse IgG AF633, anti-rabbit AF488), conjugated with fluorophore were applied (1 h, room temperature) for fluorescence labeling. For experiments using coverslips coated with immunostained cells, immobilization was carried out using Mowiol 4.88 (supplemented with DAPI) on microscope slides. Cells seeded onto confocal chamber slides were stained for chromatin using Hoechst 33342 or DAPI as indicated in the figures.

Western blot

Cells were lyzed and suspended with 95°C 1x Laemmli-buffer supplemented with 1 mM DTT. No DTT was added for non-reducing Western blot samples (Figures S13C and S13D). Samples were incubated at 95°C for 10 minutes and loaded onto SDS-polyacrylamide gels (Mini-Protean TGX gels 4-20%, Bio-Rad). Following gel electrophoresis, proteins were transferred onto nitrocellulose membranes. Blocking was achieved using TBST containing 5% BSA for 1 h at room temperature. Primary antibodies (anti-hSSB1 HPA044615 or anti-GAPDH G9545) were applied overnight in blocking reagent at 4°C. HRP-conjugated secondary antibodies (Peroxidase AffiniPure Goat Anti-Rabbit or Anti-Mouse IgG) were applied for 1 h at room temperature. Immobilon Crescendo Western HRP substrate was used for chemiluminescence-based image development. Images were captured on a Bio-Rad ChemiDoc imaging system.

Epifluorescence and confocal microscopy of immunostained cells

For epifluorescence microscopy, a Zeiss Cell Observer Z1 microscope was used with a plan-apochromat 63x oil immersion objective with a numerical aperture of 1.46. 12-bit images were captured at a pixel size of 1388 x 1040. LED module light sources were used for excitation at 385 nm, 475 nm, and 630 nm with excitation/emission filter setups of 335-383/420-470, 450-490/500-550, 625-655/665-715 nm, respectively. An AxioCam MR R3 camera (Zeiss) was used for fluorescence detection.

For confocal microscopy, a Zeiss LSM 800 microscope was used with a plan-apochromat 63x oil immersion objective with a numerical aperture of 1.40. 16-bit images were obtained at 1437x1437 pixel size. For excitation, 405 nm, 488 nm, and 640 nm wavelength laser lights were used with pinhole sizes of 1 Airy unit in each case. GaAsP photomultiplier tubes were used for fluorescence emission detection. Imaging and 3D reconstruction were performed using ZENPro software.

Colocalization analysis

Colocalization analysis was performed on confocal images using ImageJ. Mean intensity of G3BP1 inside SGs was measured and thresholds on the red channel were set as the minimum of the observed mean intensity of G3BP1 droplets. Thresholds on the green channel were set similarly, as the minimum of the observed mean intensity of hSSB1 inside SGs. Since hSSB1 has a high nuclear signal, nuclei were deleted from green channel images before thresholding. The thresholded images were used for calculating Manders split and object-based colocalization coefficients. Manders coefficient is proportional to the amount of fluorescence of the colocalizing pixels in each color channel. Values range from 0 to 1, expressing the fraction of intensity in a channel that is located in pixels where there is above-threshold intensity in the other color channel. Object-based colocalization analysis shows the ratios of centers of mass coincidence for particles detected in both channels using the thresholds described above. The analysis described above was performed using the JaCoP plugin in ImageJ.[62]

Determination of nuclear hSSB1 intensities and the number of SGs per cell

Using the microscopy setup described above, we obtained tile images at each different condition in order to achieve a sufficient sample size of around 60 cells per image. The tiles were stitched together using ZENPro. Nuclei were detected as ROIs based on DAPI/Hoechst signal. Integrated pixel density of hSSB1 signal was measured on nuclear ROIs and normalized to indicated controls.

SGs were counted on individual images according to G3BP1 signal, and SG counts were divided by the number of nuclei detected as ROIs in the given images based on DAPI/Hoechst staining. Thus, an average SG number per cell was determined from each individual image.

Cell typization

To determine whether hSSB1 overexpression or silencing influences the fraction of cells forming stress granules (SG+), we devised a method to quantify the number of SG+ cells upon H_2O_2 treatment when either EGFP or hSSB1-GFP is overexpressed, or endogenous hSSB1 is silenced. Using the epifluorescence microscopy setup described above, we obtained tile images at each condition in order to achieve a sufficient sample size. Tiles were stitched together using ZENPro, and the full image was equally divided into 4 subimages, which were analyzed separately. Outlines of cells were detected based on G3BP1 signal using Cellpose deep learning-based algorithm.[63] The detected outlines

were imported to ImageJ as ROIs. Thus, each ROI represented a different cell in the image. Mean intensity, Skewness and Kurtosis (third and fourth order moment about the mean) were measured on ROIs. A cell was considered as EGFP+ if its mean fluorescence intensity in the green channel was higher than the mean intensity of the predetermined green autofluorescence of a HeLa cell in the applied imaging setup. Skewness and Kurtosis was indicative of the heterogenous distribution of the G3BP1 fluorescence signal in the cytoplasm. The more SGs were seen, the higher Skewness and Kurtosis values were obtained. Thus, a cell was considered SG+ if both Skewness and Kurtosis were higher than their predetermined thresholds of 1 and 5, respectively. Cell typization was done on all 4 subimages ($n = 4$) at the given condition. Means $\pm$ SEM (standard error of mean) values are reported.

QUANTIFICATION AND STATISTICAL ANALYSIS

Amino acid sequence alignment was performed in Ugene using ClustalW. Data analysis and visualization was performed using OriginPro 2018. Pixel densitometry of electrophoretic gels and immunoblots was performed using GelQuant Pro software v12. Statistical analysis was performed in OriginPro 2018. Statistical tests and significance levels are indicated in the figure legends.